

Thymosin β 4 is an Endogenous Iron Chelator and Molecular Switcher of Ferroptosis

Joanna I. Lachowicz

University of Cagliari, Cittadella Universitaria

Giuseppe Pichiri (✉ pichiri@unica.it)

University of Cagliari, Cittadella Universitaria

Marco Piludu

University of Cagliari, Cittadella Universitaria

Sara Fais

University of Cagliari

Germano Orrù

University of Cagliari

Terenzio Congiu

University of Cagliari, Cittadella Universitaria

Monica Piras

University of Cagliari, Cittadella Universitaria

Gavino Faa

University of Cagliari, Cittadella Universitaria

Daniela Fanni

University of Cagliari, Cittadella Universitaria

Gabriele dalla Torre

Kimika Fakultatea, Euskal Herriko Unibertsitatea UPV/EHU, Donostia International Physics Center (DIPC)

Xabier Lopez

Kimika Fakultatea, Euskal Herriko Unibertsitatea UPV/EHU, Donostia International Physics Center (DIPC)

Kousik Chandra

King Abdullah University of Science and Technology (KAUST)

Kacper Szczepski

King Abdullah University of Science and Technology (KAUST)

Lukasz Jaremko

King Abdullah University of Science and Technology (KAUST)

Mitra Ghosh

King Abdullah University of Science and Technology (KAUST)

Abdul-Hamid Emwas

King Abdullah University of Science and Technology (KAUST)

Castagnola Massimo

National Research Council (Consiglio Nazionale delle Ricerche)

Mariusz Jaremko

King Abdullah University of Science and Technology (KAUST)

Ewald Hannappel

University of Erlangen-Nuremberg

Pierpaolo Coni

University of Cagliari, Cittadella Universitaria

Research Article

Keywords: Thymosin β 4, anti-inflammatory, neurodegeneration, macrophage cell, tissue degeneration

Posted Date: July 9th, 2021

DOI: <https://doi.org/10.21203/rs.3.rs-677051/v1>

License:  This work is licensed under a Creative Commons Attribution 4.0 International License. [Read Full License](#)

Abstract

Thymosin $\beta 4$ (T $\beta 4$) was extracted forty years ago¹ from calf thymus. Since then, it has been identified as a G-actin binding protein involved in blood clotting, tissue regeneration, angiogenesis, and anti-inflammatory processes. T $\beta 4$ has also been implicated in tumor metastasis and neurodegeneration. However, the precise roles and mechanism(s) of action of T $\beta 4$ in these processes remain largely unknown, with the binding of the G-actin protein being insufficient to explain these multi-actions. Here we identify for the first time the important part of T $\beta 4$ mechanism in ferroptosis, an iron-dependent form of cell death, which leads to neurodegeneration and somehow protects cancer cells against cell death. Specifically, we demonstrate four iron²⁺ and iron³⁺ binding regions along the peptide and show that the presence of T $\beta 4$ in cell growing medium inhibits erastin and glutamate-induced ferroptosis in macrophage cell line. Moreover, T $\beta 4$ increases the expression of oxidative stress-related genes, namely BAX, hem oxygenase-1, Heat shock protein 70 and Thioredoxin reductase 1, which are downregulated during ferroptosis. We state the hypothesis that T $\beta 4$ is an endogenous iron chelator and take part of iron homeostasis in ferroptosis process. We discuss the literature data of parallel involvement of T $\beta 4$ and ferroptosis in different human pathologies, mainly cancer and neurodegeneration. Our findings confronted with literature data shows that controlled T $\beta 4$ release could command on/off switching of ferroptosis, and may provide novel therapeutic opportunities in pathologies of cancer and tissue degeneration.

Introduction

Ferroptosis is an iron-dependent oxidative form of cell death that is morphologically, biochemically, and genetically distinct from other non-apoptotic cell death processes². The latest definition of ferroptosis was presented in 2018 by the Nomenclature Committee on Cell Death (NCCD)³ as '*a form of regulated cell death (RCD) initiated by oxidative perturbations of the intracellular microenvironment that is under constitutive control by GPX4 and can be inhibited by iron chelators and lipophilic antioxidants. Ferroptosis initiates with lipid peroxidation due to ROS generation and iron availability*'. Ferroptosis lead to morphological changes with a necrotic morphotype (i.g. predominant mitochondrial shrinking, an electron-dense ultrastructure, reduced/disappeared cristae, and ruptured outer mitochondrial membrane)³. Ferroptotic cell death is thought to require mutation of the oncogenes HRAS, KRAS, or BRAF, and is caused by lethal iron-dependent lipid peroxidation^{4,5}. To provoke cell death, ferroptosis likely requires continuous iron-dependent ROS production over a prolonged period of time, which can be observed in neuronal, cardiac, and hepatic cells, when exposed to high iron concentrations in neurodegeneration pathology⁶, ischemic conditions⁷ and hepatic chromatosis⁸, respectively.

Iron, a highly redox-reactive element, is required in a variety of biological processes. Cancer cells develop different mechanisms both to uptake high quantities of iron, and to protect themselves against iron toxicity⁹. Activation of the ferroptosis supresses tumor cell growth and successively leads to cell death. The controlled on/off switching of ferroptosis may provide novel therapeutic opportunities in pathologies of cancer and tissue degeneration, respectively.

Thymosin $\beta 4$ (T $\beta 4$) is a G-actin binding protein with different functions in the human body, including blood clotting¹⁰, tissue regeneration¹¹, angiogenesis¹², prenatal and early childhood development¹³ and tumor metastasis¹⁴. T $\beta 4$ is also involved in anti-inflammatory and neurodegenerative processes¹⁵. At the subcellular level, T $\beta 4$ is localized in the cytoplasm¹⁶ and/or nucleus¹⁷, and can be translocated between compartments after induction^{17,18}. Thymosin $\beta 4$ -overexpression is correlated with different human cancer types e.g., pancreatic¹⁹ and colorectal cancer²⁰ and T $\beta 4$ is considered a potential molecular target for anticancer therapy. Indeed, T $\beta 4$ gene silencing decreases stemness and invasiveness in glioblastoma²¹, and suppresses proliferation and invasion of non-small cell lung cancer cells²².

The exact mechanisms of T $\beta 4$ action are still unknown. Recently, we hypothesized that the regulatory function of T $\beta 4$ in numerous physiological processes is correlated with its potential essential metal – binding ability²³. Here, we discuss for the first time the formation of metal complex with T $\beta 4$ and its biological importance in ferroptosis. We observed that an increased concentration of T $\beta 4$ can effectively inhibit the ferroptosis process, a mechanism which is used by cancer cells with enhanced T $\beta 4$ expression. The inhibition of ferroptosis by augmenting extracellular concentrations of T $\beta 4$ can stop cell degeneration, and such a strategy could be used in therapy.

Results

Thymosin $\beta 4$ metal coordination.

Thymosin $\beta 4$ is a 43 amino acid peptide with acetylated N-terminus. It is an acidic peptide (pI 5.1) due to the presence of 11 amino acids with carboxylic groups in the side chain, which are the potential metal binding sites²⁴. Moreover, nine lysine residues in the primary sequence have high affinity to transition metal ions²⁴. Thymosin $\beta 4$ has no secondary structure in water, while in hydrophilic environment two alpha-helices are formed in the 5–17 and 30–39 regions²⁵.

To our knowledge, no experimental or molecular dynamics study of the formation of essential metal complexes has been performed with T $\beta 4$, despite there being numerous potential metal-binding sites. In order to investigate the metal binding sites in the T $\beta 4$ peptide, we chose nuclear magnetic resonance (NMR) techniques, which deliver valuable structural data of metal complexes²⁶.

The interaction of iron ions with T $\beta 4$ in water was investigated in a residue-specific manner by monitoring of 2D ¹³C-¹H HSQC (heteronuclear single quantum coherence) NMR (Figure S1, S2, S3, S5, S6), focused on the aliphatic region. The overlay of the HSQC data (Figure S2, S3, S5 and S6) showed that metal/peptide interactions are nonspecific, and there is no structural change upon interaction with iron²⁺ nor iron³⁺ ions.

The presence of metal ions in the peptide solution leads to the lowering of the peptide signals. The comparative analysis of the peptide signal pattern with and without metal ion permits the isolation of amino acids affected by the interactions with the metal ions (Figure S4 and S7). In the thymosin solution

containing iron²⁺ and iron³⁺ ions, eighteen and fifteen residues respectively (Table 1) showed a major drop in intensity. Since iron³⁺ is paramagnetic, we observed greater overall signal broadening of the residues, with the aforementioned residues showing major drops in intensity.

Circular dichroism (CD) structural analysis of free Tβ4 in water showed that the secondary structure is mainly unorganized, and only 20% could be associated to the helical form. The addition of iron ions to the peptide solution did not significantly change the secondary structure (Figure S9).

Table 1
Amino acid residues affected by metal/peptide interactions.

Binding region	I				II				III				IV						
Fe (II)	S1	K3	P4	M6		K11	F12	D13	S15	L17	T22	P27	L28	P29	S30	T33	I34		
Fe (III)	S1	K3	P4	M6	I9		F12	D13	S15		T22		L28			T33	I34	Q35	E36
Al (III)			P4	D5	M6	I9	E10	F12	D13				L28				I34	Q35	E36

In general, NMR data precision is limited by the presence of paramagnetic species and does not permit detailed coordination analysis with iron ions. For this purpose, Al³⁺ ions, which form similar stoichiometry and geometry complexes as Fe³⁺, were used to model Fe³⁺/ Tβ4 complexes.

The analysis of the overlay HSQC data (Fig. 1) showed that metal/peptide interactions are nonspecific, and there were no structural changes in thymosin upon interaction with Al³⁺ ions.

The chemical shift perturbation (CSP) was calculated considering the free peptide form and 1:5 (peptide:metal) as the maximum stoichiometry leading to the reduction of the peptide's peak intensities and no further chemical shift changes. Only 48 isolated peaks were considered for calculating the CSP and intensity analysis. Analysis of the CSP plot (Fig. 2) showed that Al (III) ions interact with N-terminal residues of Tβ4. The residues that most likely interact with the metal ion are listed in Table 1.

Figure 2 shows that residues Ile⁹ and Gln³⁵ presented noticeable changes upon interaction with Al³⁺, however the CSP value is too small to define the metal/peptide interaction as strong and with high affinity. The plot of signal intensities as a function of the Tβ4:metal ratio showed a consistent decrease for most of the residues in 1D (Fig S12) and in 2D (Figure S13). However, it is important to note that the intensity of 1D spectra is directly proportional only to the population, while the 2D spectra intensity is modulated by many different factors.

The diffusion NMR data at the different metallopeptide ratios showed the presence of only one species with a diffusion constant 1.25e¹⁰ m²/sec.

The NMR data analysis showed that metal ions interact with numerous amino acid residues, and four metal binding sites could be distinguished within the Tβ4 structure (namely I-IV, Table 1). The binding modes within four metal binding sites were modelled with the density functional theory (DFT) calculation.

Tβ4 contains 11 acidic residues: eight glutamate and three aspartate residues¹. According to Pearson's hard and soft acids and bases (HSAB) principle, hard metal ions (Fe³⁺ and Al³⁺) show preference for binding hard bases, such as the negatively charged carboxylate side chains of glutamate and aspartate amino acids. Although there can be other donors to hard metal ions, such as backbone carbonyl and amide groups of proteins, by virtue of the partial covalent nature of the coordination bond, these donors are less competitive. Indeed, we recently demonstrated, from a thermodynamic perspective, that the preferred binding sites of Al³⁺ in proteins are the negatively charged side chains of amino acids rather than the backbone carbonyl and amide groups²⁸.

The chemical shift perturbation of the NMR data showed that the main changes in chemical shifts upon Al³⁺ addition arise in two different areas of the protein: within the N-terminal segment (metal binding sites I and II) and the C-terminal segment (metal binding sites III and IV).

The conformational analyses were prepared in order to build 3D models of the Al³⁺-Tβ4 complex and obtain some reliable initial configurations of this hard metal ion bound to Tβ4. According to the literature, Tβ4 in water solution exists mainly in a disordered state and it is unclear whether secondary structure elements such as extended helices in the N- and C-terminus of the protein arise upon interaction with other partners such as actin²³. Thus, in the starting structure, the Tβ4 sequence was considered "unfolded", without main secondary structure elements (helices and sheets).

Three major binding modes for the Al³⁺-Tβ4 system were obtained (Table 2): first the metal interacting with both the N- and C-terminus of the protein (Tβ4^{N-C}); second with the metal bound to the N-terminal and in the middle of the protein (Tβ4^{N-mid}); third with the metal bound only in the N-terminus of the protein (whereas the rest of the sequence remains highly disordered; Tβ4^{N-N}). Interestingly, all the three binding modes featured four negatively charged residues (side chains of either ASP or GLU) with a net charge of -4 surrounding the metal center, a situation that is coherent with the one proposed by Dudev and Lim²⁹, who stated that the optimal number of acetate-type donors in a metal binding site is equal to q + 1, where q is the charge of the metal, when first coordination shell residues are taken into account.

In Tβ4^{N-C} binding mode, the metal is bound to GLU⁸ and GLU²¹ in a bidentate fashion, and to ASP⁵ and GLU³⁵ by a single oxygen donor (Fig. 3A). The six oxygen donors coordinate Al³⁺ through an octahedral geometry, with O-Al-O angles ≥ 150 degrees. During the simulation, after 3μs the carboxylate side chain of GLU³⁵ coordinates the metal with both oxygen donors whereas the side chain of GLU²¹ switches to a monodentate binding mode. The original state is then restored after 4 μs up to the end of the simulation. Overall, the Tβ4^{N-N} protein-metal complex remains stable for the entire course of the simulation, and no other residues nor water molecules enter the first coordination shell of the metal.

The T β 4^{N-mid} binding mode is characterized by Al³⁺ ions coordinated to the side chains of ASP² and ASP⁵ in a monodentate fashion, and to the side chains of GLU¹⁰ and GLU²⁴ in a bidentate fashion (Fig. 3B). Also in this case there is no change in the coordination pattern of T β 4^{N-mid} during the entire simulation time of 5 μ s.

Finally, the T β 4^{N-N} binding mode displayed an octahedral geometry, in which the first coordination shell of the metal is filled by one oxygen donor from the side chains of ASP⁵ and GLU⁸ and two oxygen donors from the side chains of ASP² and GLU¹⁰ (Fig. 3C). The metal center maintains this binding mode for the whole simulation.

Structural characterization revealed that T β 4^{N-N} displays the highest degree of disorder less compaction rate with the average root mean square deviation (RMSD) and radius of gyration (Rg) of 1.07 and 1.29, respectively, compared to T β 4^{N-mid} (0.89 and 1.11, respectively) and T β 4^{N-C} (0.92 and 1.15, respectively) as reported in Table S1. This is coherent with the fact that, in the case of T β 4^{N-mid} and T β 4^{N-C}, the N- and C- termini are closer due to their respective metal binding modes that involve residues either in the medial or distal region of the protein, as also highlighted by their shorter end to end distance compared to T β 4^{N-C} (Table S1). The average amount of intramolecular hydrogen bonds is similar for T β 4^{N-C} and T β 4^{N-N} and slightly higher for T β 4^{N-mid} (Table S1); most populated H-bonds and salt bridges for each binding mode are reported in Table 2.

As can be deduced from Table S2, all three metal-T β 4 complexes exist mainly as random coil structures; the prevalent structural motifs are bends and turns, consistent with the disordered nature of T β 4. Interestingly, T β 4^{N-C} and T β 4^{N-mid} display a similar β -sheet content (16.8 and 17.6 %, respectively), whereas T β 4^{N-N} shows a much lower content of this structural motif (2.5 %). On the other hand, the latter binding mode displays a higher helicity propensity compared with the other two, in particular it features 94.1 % of the 3₁₀-helix motif. Such a situation could be due to the fact that the metal binding activity of T β 4^{N-N} is confined to the N-terminal segment of the protein, while the remaining sequence is highly disordered and may increase the propensity to form helical patterns in its C-terminal regions.

Table 2
Percentage of hydrogen bond and salt bridge occupancies during the simulations. *bb*: backbone, *sc*: side chain.

TB4 ^{N-C}			TB4 ^{N-mid}			TB4 ^{N-N}		
Donor	Acceptor	Occ. (%)	Donor	Acceptor	Occ. (%)	Donor	Acceptor	Occ. (%)
GLU ³⁵ -N _{bb}	THR ³³ -O _{sc}	27.6	LYS ³⁸ -N _{bb}	GLU ³⁵ -O _{bb}	26.0	THR ²² -N _{bb}	LYS ¹⁹ -O _{bb}	23.8
LEU ¹⁷ -N _{bb}	LYS ¹⁴ -O _{bb}	25.8	LEU ²⁸ -N _{bb}	ASN ²⁶ -O _{sc}	28.2	GLN ²³ -N _{bb}	LYS ¹⁸ -O _{bb}	22.2
LEU ²⁸ -N _{bb}	ASN ²⁶ -O _{sc}	36.6	ILE ³⁴ -N _{bb}	LYS ³¹ -O _{bb}	26.7	GLU ²¹ -N _{bb}	LEU ¹⁷ -O _{bb}	23.4
THR ³³ -N _{bb}	GLN ³⁶ -O _{bb}	32.0	LYS ³¹ -N _{bb}	LEU ²⁸ -O _{bb}	21.1	ILE ⁹ -N _{bb}	MET ⁶ -O _{bb}	53.0
LYS ³¹ -N _{bb}	LEU ²⁸ -O _{bb}	22.5				GLU ⁸ -N _{bb}	ASP ⁵ -O _{bb}	51.5
						LYS ³⁸ -N _{bb}	GLU ³⁵ -O _{bb}	20.0

All three binding modes are quite stable across the 5 μ s time scale. We also observed that T β 4 binding to aluminium could affect the overall secondary structure pattern of the thymosin. Since both glutamate and aspartate residues are the preferred acidic groups of hard metals, the three binding modes characterized herein could fit either Al (III) or Fe (III) metal ions.

Thymosin β 4 and ferroptosis

Iron is an essential metal ion with a fundamental role in diverse cellular processes, such as DNA synthesis, proliferation, cell cycle regulation, and the function of proteins containing iron-sulphur clusters³⁰. Iron-sulphur cluster-containing proteins include enzymes that contribute to maintaining genomic stability, as well as respiratory function³⁰. Indeed, rapidly reproducing cancer cells re-programme iron metabolism in ways that result in net iron influx^{9,30}. Iron is a highly reactive metal due to its redox potential, and when present in a free ion form, it contributes to the production of reactive oxygen species (ROS) in the Fenton reaction (Scheme 2). Oxidative and iron-dependent cell death with neurodegenerative consequences was previously described in epilepsy, stroke, and other trauma situations³¹⁻³³. Importantly, increased levels of iron were found in the central nervous system of patients with neurodegeneration⁶. Surprisingly, elevated iron concentrations in cancer cells do not lead to cell disruption, but the exact mechanism of cell defense remains unknown.

Macrophages, together with hepatocytes, play key roles in iron metabolism by mediating iron storage and recycling³⁴. In hereditary haemochromatosis (HH), a representative disease that causes iron overload, hepatocytes are the first site of iron accumulation^{35,36}. Recent studies^{37,38}, showed that pathological iron overload in mouse macrophage cell line J774 induces ferroptosis and subsequent cell destruction. Therefore, we used J774 cells as a model to study the importance of macrophages in iron metabolism³⁹, and their consequent susceptibility to ferroptosis.

Ferroptosis can be induced *in vivo* in rat hippocampal slices and primary oligodendrocyte models as well as in ischemia-reperfusion injury models, by high concentrations of extracellular iron or glutamate, or by depletion of extracellular cysteine. *In vitro*, ferroptosis can be induced by physiological conditions (e.g., high extracellular iron or glutamate) or small molecules (e.g., Erastin), which blocks system X_c⁻-mediated Cys₂ import² (heterodimer composed of solute carrier family 7, member 11 (SLC7A11) and SLC3A2; Scheme 2), while glutamate receptors are not involved in ferroptosis⁴⁰. Erastin and glutamate are termed

type I ferroptosis inducers that inhibit cysteine uptake by the cysteine/glutamate antiporter (system x_c^-), enabling glutathione synthesis (Scheme 2), and thereby lowering antioxidant defenses⁴.

Glutamate-induced oxidative stress leads to lipid peroxidation-mediated ferroptosis (Scheme 2) and is a major contributor to neurodegenerative pathologies⁴¹. In recent studies, L-Glutamate (3h, 5mM) mimicked *in vitro* the consequences of stroke and neurodegenerative pathologies in cell cultures^{42,43}. The addition of iron enhances glutamate induced cell death⁴¹, while inhibition of ferroptosis prevents glutamate-induced cell death in organotypic hippocampal slice cultures⁴. Importantly, glutamate activity can be inhibited by iron chelators (e.g., Desferal)⁴.

We induced ferroptosis in J774 cells in separate experiments by the addition of Erastin or glutamate and monitored the increase of free radicals with the BODIPY-C11 fluorescence marker (Fig. 4). 4,4-Difluoro-5-(4-phenyl-1,3-butadienyl)-4-bora-3a,4a-diaza-s-indacene-3-undecanoic acid (C11-BODIPY^{581/591}) is a fluorescent probe ($\lambda_{ex} = 510$ nm; $\lambda_{em} = 595$ nm) used for evaluating lipid peroxidation and antioxidant efficacy in model membranes, lipoproteins, biological fluids, and living cells⁴⁴, and has been used in ferroptosis studies⁴.

After 24 h treatment with type I ferroptosis inducers (i.e., glutamate and Erastin), we observed a decrease in the green fluorescence light, while there was no change in fluorescence intensity in either the control nor the T β 4 sample (Fig. 4). Notably, samples supplemented with glutamate (or Erastin), and successively with T β 4 after 4h, showed the same fluorescence intensity after 24 h as the control sample.

Ferroptosis was primarily characterized by condensed mitochondrial membrane densities and smaller mitochondria, as well as diminished or absent mitochondria crista, and ruptured outer membrane⁴⁶. Recent studies divided mitochondrial morphological alterations into three categories according to the whether the mitochondria were fragmented or not, and whether they accumulated around the nucleus. Cells with a network of elongated mitochondria were assigned to category I, uniform-distributed fragmented mitochondria in cells were classified as category II, and cells with fragmented mitochondria mainly accumulating around the nucleus were classified as category III⁴⁶⁻⁴⁹. Mitochondrial morphological changes and metabolic regulation, especially the energetic, iron and aliphatic acid metabolism involved in ferroptosis, were extensively described in a recent review⁵⁰.

For a more detailed characterization of glutamate-induced ferroptosis in J774 cells, including T β 4 inhibition, we evaluated the morphological changes by TEM microscopy. The results obtained from this ultrastructural analysis are summarized in Fig. 5 (and Figure S19), 6 and 7, showing cells from different experimental groups. In the control group (Figs. 5A and 5B), the J774 cells appeared normal at the ultrastructural level. They were mainly characterized by a well-developed Golgi apparatus, rough endoplasmic reticulum, and the presence of numerous mitochondria. The nuclear compartment was separated from the cytoplasm by the double membrane of the nuclear envelope, and the cells appeared to be in interphase due to the presence of both heterochromatin and euchromatin. The presence of condensely packed chromatin and the absence of the nuclear envelope represented the main features of mitotic cells, which were often observed in control samples (Figure S19).

Administration of T β 4 (Fig. 5C, D) did not appear to alter cell morphology: samples displayed structural integrity of all their cellular compartments and organelles including mitochondria.

Following glutamate (Fig. 6A and 6B) and Erastin (Fig. 7A and 7B) treatments, the cellular morphology of the J774 cells was dramatically altered. Specific ultrastructural alterations were mainly observed in the cytoplasmic compartment, where numerous mitochondria were found accumulating around the nucleus. These cellular organelles appeared drastically altered, showing mitochondrial membrane rupture and evident cristae disorganization. Moreover, the presence of lysosomal activity and disruption of the Golgi apparatus and rough endoplasmic reticulum indicated a poor cellular condition. However, none of these morphological alterations were related to an apoptotic form of cell death. Indeed, during our TEM investigation, no nuclear alterations were detected, and the nucleus appeared surrounded by a continuous nuclear envelope, displayed an evident nucleolus and well-organized chromatin, and no chromatin condensation or margination were detected in the J774 cells after either glutamate or Erastin treatments. Moreover, both Erastin and glutamate treatment seemed to induce cell detaching and a rounded cellular shape (Fig. 6A). Their cell surface appeared continuous without any signs of plasma membrane rupture or disorganization, although we did observe thin protrusions. Most of these appeared to be continuous tunnelling nanotubes connecting neighboring cells (Fig. 6A, asterisk) previously described as structures involved in intercellular communication^{51,52}.

Administration of T β 4 in glutamate (Fig. 6C and 6D) and Erastin (Fig. 7C and 7D) treated samples seemed to gradually reverse the alterations described above. The cytoplasmic compartment showed reorganization of its cellular structures associated with an evident diminishing of lysosomal activity. Mitochondria showed partially reconstituted cristae and a continuous mitochondrial membrane. The rounded cell shape transitioned to a more flattened type.

Interestingly, in the glutamate and Erastin-treated cells we frequently detected the presence of tunnelling nanotubes (TNT) connecting neighboring cells (Fig. 7A, asterisk). TNT are considered dynamic structures whose formation and organization can be affected by different pathological conditions. It has been reported that oxidative stress may induce TNT formation in astrocytes and hippocampal neurons⁵³. Inflammation and even viral infections have been observed to spread via tunnelling nanotubes. And they may also be involved in the cell-to-cell transfer of signal transduction molecules. Fas ligand (FasL) involved in programmed cell death has been demonstrated to stimulate TNT formation, promoting propagation of cell death signals to neighboring cells⁵⁴. Our results suggest a possible involvement of the ferroptotic process in the cell surface reorganization and TNT formation, which may facilitate diffusion of the ferroptosis process between connected cells. Considering that tunnelling nanotubes are F-actin containing protrusions of the cell surface, T β 4 could modulate ferroptosis not only by its metal binding sites, as described above, but also through its G-actin binding properties. T β 4, as a major G-actin sequestering protein, could prevent tunnelling nanotube formation in Erastin and glutamate treated J774 cells inhibiting propagation of ferroptotic cell death signals to the connected cells.

These morphological results clearly show that glutamate and Erastin induce ferroptosis in J774 cells, while T β 4 administration after 4 h can inhibit the process and reverse the critical cellular condition. The biochemical pathways involved in these processes were investigated by gene expression profiling.

According to Dixon², ferroptosis could be defined as a sabotage mechanism, where the cell inhibits own-normal processes. However, ferroptosis is related to oxidative stress, and consequently the involvement of oxidative stress proteins is expected. Indeed, among thirty different genes studied in relation to ferroptosis⁵⁵, many are involved in oxidative stress. In our study, we chose four genes, namely BAX (Bcl-2 associated X-protein), HSP-70 (Heat shock protein 70), which are involved in the oxidation process, but are poorly described in connection with ferroptosis; and HO-1 (heme oxygenase) and TXNRD-1 (Thioredoxin reductase 1) which were recently linked to ferroptosis.

Bax is a cytosol protein, which translocates into mitochondria when apoptosis occurs⁵⁶ (Scheme 2). Jungas et al.⁵⁷ studied glutamate toxicity and regulation in neuronal development. Their studies showed BAX-activation mechanism dependent on glutathione, with downstream effect of glutathione depletion leading to the direct activation of BAX. Moreover, Bax and its transcript increase significantly in cerebral ischemia-injured neurons^{58,59} suggesting that glutamate could be involved the mechanism of BAX expression control.

Heat shock protein 70 (Hsp70) is a stress-responsive protein increasing under stress conditions, namely heat, hypoxia, and glucose deprivation. Increased Hsp70 concentration leads to higher stress tolerance and cytoprotection⁶⁰. Hsp70-mediated cytoprotective effects were studied in vitro in numerous cell/tissue types under changing environmental conditions of stress. Noteworthy, Hsp70 have significant cytoprotective effects under ischemic conditions. For instance, induction of Hsp70 (i.g. by enforced overexpression with viral vectors or drugs) protects brain cells against ischemic injuries⁶¹⁻⁶⁴. Oxidative stress and antioxidants can influence Hsp70 expression^{65,66}, while reduction in Hsp70 expression leads to higher ROS generation and mitochondrial protein oxidation⁶⁷. Guo et al.⁶⁰ showed that Hsp70 regulates cellular redox status by changing the activities of the GSH-related enzymes, glutathione peroxidase and glutathione reductase, in response to hypoxic and ischemic stress. The switching of antioxidant enzyme activities could be critical mechanism mediating the enhanced cytoprotection afforded by enhanced expression of Hsp70. Despite numerous studies and different theories, the exact molecular mechanisms of Hsp70 action in ischemic conditions remains undefined

Heme oxygenase (HO)-1 metabolizes heme into biliverdin/bilirubin, carbon monoxide, and ferrous iron, and has been suggested to demonstrate cytoprotective effects under various stress-related conditions. HO-1 is commonly regarded as a survival molecule, exerting an important role in cancer progression, and its inhibition is considered beneficial in several cancers⁶⁸. HO-1 is often upregulated in tumor tissues, and its expression is further increased in response to therapies⁶⁹. The role of HO-1 in ferroptosis is extensively described in the recent review⁶⁸. Depletion of cellular glutathione has been shown to increase HO-1 gene transcription in the mouse motor neuron-like hybrid cells, NSC34 cells⁷⁰. The correlation between HO-1 expression and ferroptosis is unclear. In HT-1080 fibrosarcoma cells, Erastin induces a time- and dose-dependent increase of HO-1 expression⁷¹. However, HO-1 also functions as a negative regulator in Erastin- and Sorafenib-induced hepatocellular carcinoma, since knockdown of HO-1 expression enhanced cell growth inhibition by Erastin and sorafenib⁷².

The selenoprotein thioredoxin reductase 1 (TXNRD1 gene) is a cytoplasmic protein that decreases thioredoxin levels and protects against oxidative stress⁷³. Recently, it was shown that TXNRD1 is a strong negative modulator of ferroptosis susceptibility in pancreatic cancer cells⁷⁴. Moreover, a high-dose (25 mg/kg) of the anti-rheumatoid arthritis drug auranofin (AUR) upregulates hepcidin expression and induces ferroptosis and causes lipid peroxidation through inhibition of thioredoxin reductase (TXNRD) activity, in C57BL/6J mice and a mouse model of hemochromatosis (Hfe-/- mice)⁷⁵.

Here, we evaluated the levels of BAX, HO-1, Hsp70 and TRNRD-1 mRNAs (Fig. 8) under normal and ferroptosis conditions, which was induced by the extracellular overload of glutamate. In addition, we evaluated mRNA expression levels of these proteins in the presence of high extracellular concentrations of thymosin. Finally, we examined their mRNA levels in the cells treated with thymosin after 4 h of ferroptosis induction. We observed that glutamate overload led to the downregulation of all studied genes; conversely the presence of T β 4 upregulated mRNA expression, particularly of HO-1. Notably, the downregulation of glutamate could be inverted by the successive treatment with T β 4.

Discussion

Thymosin β 4 is highly conserved across the animal kingdom, from amphibians to mammals, and its amino acid sequence is well conserved¹⁶. Among mammalian species, the amino acid sequences of human, rat, murine, bovine, porcine, and ovine T β 4, are identical⁷⁶. Thymosin β 4 is encoded by the TMSB4X gene. Mouse, rat, zebrafish, frog, and pig display differential mRNA expression of TMSB4X in organs, while in humans it is widely distributed in tissues with high concentrations of different essential metal ions⁷⁷ (Scheme 3).

Iron is an essential metal ion involved in many cellular processes. In a free ion form, iron is a redox active metal, which leads to the formation of ROS in the Fenton reaction. Cancer cells have developed many different iron-regulating mechanisms, which permit them to benefit from high iron concentration without suffering from the harmful effects of free radicals. Many iron-regulating processes in tumor pathology have already been discovered⁷⁸, while others are unknown. Considering the iron-dependent etiology of ferroptosis, it is likely that some of the unknown iron-defense processes in tumor cells can inhibit ferroptosis-induced cell death.

The involvement of T β 4 in different cancer types has been widely described in recent years (Table 3). It is noteworthy that among the 13 most common cancer types (<https://www.healthline.com/health/most-common-cancers>), the nine tissues with the highest cancer incidence also have high thymosin mRNA expression (Scheme 3, Table 3), which is further enhanced in tumors (Table 3). Recently, it was shown that ferroptosis is fundamental in anti-cancer therapy, and efficient anti-cancer drugs can induce ferroptosis-cell death (Table 3).

Table 3
List of some independent research data and reviews describing Tβ4 and ferroptosis involvement in human pathologies.

Pathology	Tβ4 involvement	Ferroptosis involvement
Cancer		
Pancreatic	In pancreatic cancer cell lines and in intraductal pancreatic mucinous neoplasms with high grade dysplasia, overexpression of Tβ4 mRNA was found with increased secretion of proinflammatory cytokines ⁷⁹	Ferroptosis controls the growth of pancreatic cancer, and the regulatory mechanisms associated with ferroptosis in pancreatic cancer are summarized in a recent review ⁸⁰ .
Hepatocellular carcinoma (HCC)	Immunoreactivity for Tβ4 was detected in 30% of HCC samples. Immunostaining was homogeneous and diffusely distributed over the entire cytoplasm. In the tumor mass, no zonation pattern was observed ⁸¹ .	Ferroptosis showed tremendous promise as a therapy, especially in HCC. The role of ferroptosis in HCC, and in the diagnosis and treatment of HCC are summarized in a recent review ⁸² .
Gastric	Increased expression of Tβ4 was observed in 43.3% of gastrointestinal stromal tumors, and significantly associated with tumor size and increased mitosis ⁸³ .	The role of ferroptosis in gastric cancers, and the proteins involved in ferroptosis regulation, were recently reviewed ⁸⁴ .
Colorectal	Tβ4 is overexpressed in a side population of cancer stem cells and CD133-positive colorectal cancer stem cells ⁸⁵	Ferroptosis inducer RSL3 initiated cell death and ROS accumulation in HCT116, LoVo, and HT29 CRC cells over a 24 h time course. This effect was reversed by overexpression of GPX4 ⁸⁶ .
Breast	The cellular distribution of Tβ4 in breast cancer is heterogenous; multiple cell types within the tumor microenvironment produce Tβ4 and expression varies between tumors ⁸⁷ . In addition, hypoxia-induced Tβ4 is strongly associated with expression of hypoxia inducible factors (HIF-1 and HIF-2) and is also clinicopathologically involved in the lymph node metastatic potential of breast cancer ⁸⁸ .	Siramesine and Lapatinib treatment induce ferroptosis in breast cancer cells. The ferroptotic process could be used as a new therapeutic strategy to overcome apoptotic resistance in breast cancer ⁸⁹ .
Lung	Tissue microarray analysis showed that Tβ4 was highly expressed in lung cancer ⁷⁹ , and Tβ4 gene silencing in A549 and H1299 cells inhibited cell proliferation, migration, and invasion in vitro, and decreased tumor growth in vivo ¹⁹ .	Suppression of NFS1 cooperates with inhibition of cysteine transport to trigger ferroptosis in vitro and slow tumor growth. Therefore, lung adenocarcinomas upregulate pathways that confer resistance to high oxygen tension and protect cells from undergoing ferroptosis in response to oxidative damage ⁹⁰ .
Ovarian	Tβ4 is overexpressed in primary ovarian cancers when compared with normal controls. Tβ4 expression was also co-localized with CD133 expression in primary ovarian carcinomas, metastatic ovarian cancers from stomach cancers, and primary stomach cancers ⁸⁵ .	Ferroptosis as a new promising anti-tumor strategy in Epithelial ovarian cancer (OVCA), together with various genetic determinants of ferroptosis and their underlying mechanisms in OVCA are described in a recent review ⁹¹ .
Melanoma	Suppression of Tβ4 expression leads to decreased metastatic potential in murine B16 melanoma cells ⁹² . Moreover, Tβ4 is crucial for melanoma adhesion and invasion ⁹³ .	Ferroptosis has been described as an efficient strategy in melanoma therapy ⁹⁴ .
Head and neck	Higher TMSB4X expression is found in head and neck squamous cell carcinoma both at the RNA and protein levels. Overexpression of TMSB4X was significantly associated with poor prognosis of overall survival and recurrence-free survival. Silencing of TMSB4X expression in a HNSCC cell line reduced proliferation and invasion ability in vitro, as well as inhibited cervical lymph node metastasis in vivo ⁹⁵ .	Induction of ferroptosis in head and neck cancer cells overcomes cisplatin resistance ⁹⁶ .
Neurodegenerative disorders		
Alzheimer's Disease	In human Huntington's and Alzheimer's disease brains, Tβ4 was found markedly elevated in the cell bodies and processes of reactive microglia distributed to regions of neurodegeneration ⁹⁷ .	Inhibitors of ferroptosis, such as ferrostatins and lipoxstatins, protect from ischemic injury in mouse models in the liver, kidney, brain, and heart ^{4,46,98-101} . These inhibitors are also protective in models of degenerative brain disorders, including Parkinson's, Huntington's, and Alzheimer's diseases, as well as in other forms of neurodegeneration and traumatic and hemorrhagic brain injury ^{100,102-108} .
Huntington's Disease	The detailed analysis of Huntington's brains revealed that Tβ4 immunoreactivity in reactive microglia was particularly increased during the early stages of pathology ⁹⁷ .	
Other pathologies		
Stroke	After injury, Tβ4 is released by platelets, macrophages, and many other cell types to protect cells and tissues from further damage and reduce apoptosis, inflammation, and microbial growth ¹⁰⁹ . Tβ4 promotes remodeling of the CNS/PNS post-neural injury and thereby improves neurological recovery ¹¹⁰⁻¹¹³	The role of ferroptosis in stroke has been recently reviewed ¹¹⁴⁻¹¹⁶ .

Pathology	Tβ4 involvement	Ferroptosis involvement
Traumatic brain injury (TBI)	Tβ4 may have a role in the repair and remodeling of injured tissues following a hypoxic insult as indicated by a study of focal brain ischemia following occlusion of the middle cerebral artery in rats ¹¹⁷ . Tβ4 may also have a role in neuronal development and remodeling, and transcription of the gene that encodes Tβ4 is upregulated during hypoxia ¹¹⁸	The role of ferroptosis in TBI is described in recent reviews ¹¹⁹⁻¹²¹ .
Myocardial infarction	Administered immediately following a myocardial infarction in mice, Tβ4 protects heart tissue from cell death and enables heart myocytes to survive after hypoxia ¹²²	GPX4 downregulation during myocardial infarction contributes to ferroptosis in cardiomyocytes ¹²³ . Moreover, ferroptosis is involved in diabetes myocardial ischemia/reperfusion injury through endoplasmic reticulum stress ¹²⁴
Ischemia/reperfusion (I/R)	Intervention with Tβ4 after ischemia can reduce the neurological deficits in rats ¹²⁵ . Tβ4 reduced damage after ischemic heart injury, protected post hypoxic cardiac tissue, decreased infarct size, reduced scar volume, decreased inflammation, promoted angiogenesis, and improved ventricular function, and survival ^{122,126,127} .	Inhibitors of ferroptosis, e.g., Galangin ¹²⁸ and Carvacrol ¹²⁹ mitigate ferroptosis and have a neuroprotective effect in I/R.
Liver injury and fibrosis	Patients with liver diseases have serum Tβ4 levels negatively correlated with liver function ¹³⁰ . Exogenous Tβ4 administration ameliorated ischemia reperfusion-induced hepatic injury in mice ¹³¹ , and prevented in vitro acute liver injury and subsequent fibrosis through alleviating oxidative stress and inflammation ¹³²	Ferroptosis plays a crucial role in chronic intermittent hypoxia-induced liver injury ¹³³ . The connection between ferroptosis and non-cancer liver diseases are intricate and compelling ¹³⁴

Neurodegeneration is characterized by neuronal cell death. Detailed biochemical and morphological studies of neuronal tissues have linked neurodegeneration with increased iron concentrations in the tissue and successive production of free radicals ^{135,136}. Since ferroptosis was first described in 2012 ⁴, numerous research data have correlated neurodegenerative processes with iron-ROS induced cell death (Table 3), and glutamate induced cell injury ¹³⁷. Up to now, Tβ4 has never been linked to ferroptosis, but different experimental studies have shown the beneficial effects of Tβ4 in neurodegeneration (Table 3).

Ferroptosis, in contrast to other RCDs processes can be inhibited, thus inhibiting molecules- namely iron chelators and lipophilic antioxidants, could be used as a molecular switcher of the entire process. Our metal coordination studies showed that Tβ4 can bind both Fe²⁺ and Fe³⁺ metal ions in vitro in four different metal binding regions (Fig. 3). Iron chelating ability of Tβ4 takes a part of iron cellular homeostasis, and increased concentration of Tβ4 leads to upregulation of HO-1 protein expression (Fig. 8B), which metabolizes heme into ferrous iron.

Tβ4 as endogenous iron chelator influences anti-oxidative processes related to free iron ions and ROS production in Fenton reaction. Increased concentration of Tβ4 enhances expression of oxidative stress-related genes: BAX, HSP70 and TRNRD-1, which are downregulated during ferroptosis. Noteworthy, the expression of these genes is even higher when Tβ4 concentration increases during the ferroptosis process (Fig. 8A and 8D). Such observation suggests that Tβ4 expression and/or supplementation could be used to enhance anti-oxidative processes, and further inhibits ferroptosis.

In our experimental conditions, erastin- and glutamate-induced ferroptosis leads to different ultrastructural alternations of cell morphology (Fig. 6A and 6B, Fig. 7A and 7B). Some of them, i.g. those involving mitochondria, were previously described in ferroptosis processes, while the others- disruption of Golgi apparatus and rough endoplasmic reticulum, continuous tunnelling nanotubes connecting neighboring cells- are less investigated in this context and need further studies. Importantly, Tβ4 administration during ferroptosis can gradually reverse the morphological alternations (Fig. 6C and 6D, Fig. 7C and 7D).

Conclusions

Thymosin β4 is an iron chelator, which takes part of iron homeostasis mechanism and iron-related oxidative stress. Administration of Tβ4 enhances expression of oxidative stress genes (HO-1, BAX, HSP70 and TRNRD-1), which are suppressed by glutamate-induced ferroptosis. The characteristic morphological alternations of ferroptosis process (i.g. predominant mitochondrial shrinking, an electron-dense ultrastructure, reduced/disappeared cristae, and ruptured outer mitochondrial membrane) can be reversed by the administration of Tβ4, which restores normal cytoplasmic compartment organization. In this context, Tβ4 can be considered a ferroptosis switcher. A better understanding of Tβ4 pathological functioning in cancer cells, and its beneficial effects in neurodegeneration, will enable us to switch different pathological states into physiological processes.

Experimental Procedures

Reagents

Erastin, L-Glutamate, BODIPY-C11, formaldehyde, glutaraldehyde in 0.1 M sodium cacodylate buffer pH 7.4, osmium tetroxide, uranyl acetate, ethanol and xylene were Sigma Aldrich products; purity 99% and were used without further purification.

EPR experimental details

All EPR spectra were recorded using a continuous wave Bruker ELEXSYS E500 electron paramagnetic resonance (EPR) spectrometer operating at the X band equipped with a superhigh Q (ER 4122 SHQ) resonator. To create comparable data, the spectra were measured using the same conditions with instrumental parameters as describes previously^{138,139}. Bruker Xenon software (Bruker BioSpin, Rheinstetten, Germany) was used for both data collection and spectral processing.

NMR

NMR samples were prepared by dissolving 1.0 mg of T β 4 in 500 μ L of D₂O. The pD was adjusted by adding DCl or NaOD and calculated as pD = pH[pHmeter reading] + 0.4¹⁴⁰. All NMR experiments were performed on 800 MHz spectrometers equipped with a triple resonance TCl probe and Z gradients coils. The temperature was kept at 25°C and it was calibrated with an external standard mixture of ethylene glycol and DMSO-D₆ by monitoring the chemical shift difference between the hydroxyl and methylene proton. The chemical shifts were calibrated with respect to standard DSS for proton, and ¹³C chemical shifts were calibrated indirectly. D₂O was used for locking.

Apart from the one-dimensional spectrum with water suppression using excitation sculpting, two-dimensional homonuclear TOCSY, NOESY, hetero-nuclear HSQC and HSQC-TOCSY (with mixing 16 ms) experiments were recorded. For the heteronuclear experiments, 2048 and 360 data points were collected in proton and carbon dimensions, respectively, which corresponds to 125 ms and 17ms acquisition time in the respective dimension. The data were apodized with sine function and zero filled with 4096 and 1024 points in proton and carbon dimensions, respectively. The recycle delay was kept for 1 and 1.5 seconds respectively for HSQC and TOCSY-HSQC. The total measurement time was 300 and 240 minutes for HSQC and TOCSY-HSQC, respectively. The sample was stable during measurement.

Five different samples were prepared with the addition of individually FeCl₂ and FeCl₃ with Thymosin: metal ion ratios 1:0.05, 1:0.1, 1:0.2, 1:0.5, and 1:1; and five different samples were prepared with the addition of AlCl₃ with T β 4: metal ion ratios 1:0, 1:1, 1:2, 1:5 and 1:10. For the sample with some AlCl₃, slightly visible precipitation was noticed.

All NMR data were processed using Topspin 4.0.7 and analyzed with Sparky software. Nearly complete assignments of the ¹H and ¹³C resonances for all the residues were done by application of a standard and well-established procedure using HSQC and TOCSY-HSQC¹⁴¹. We also used the PROSECCO (PROtein SEquences and Chemical shift Correlations) server, which predicts the chemical shift of both folded and unfolded proteins, which is sequence-based. Since T β 4 is intrinsically disordered in D₂O, we used the server accordingly. The earlier assignment of the apo form of T β 4 was transferable.

DFT

System setup and conformational analysis

Conformational analyses were carried out on the full length N-acetylated Thymosin β -4. The protein sequence was built with Maestro v. 12.5 as a random coil (no secondary structure elements) aminoacid sequence, as this is the most likely T β 4 structure in solution²³. An acetyl group is added to the N-terminal serine residue, whereas the C-terminal serine residue is taken in its charged COO⁻ state, in agreement with the physiological form of T β 4²³. Therefore, the initial system is composed of the random coil protein and one Fe³⁺ metal ion, placed nearby the protein. The system was modeled with the OPLS-AA force field¹⁴² as implemented in the MacroModel v12.4 package. Choice of the metal ion is dictated by the absence of Al³⁺ parameters in this force field. the MacroModel v12.4¹⁴³ module was used along with the MonteCarlo Multiple Minimum (MCM) algorithm¹⁴⁴. Three different conformational analyses were performed; in the first one, the number of search iterations was set to 50000 steps and the Polak-Ribiere Conjugate Gradient (PRCG) minimization algorithm was used¹⁴⁵ set to 10000 minimization steps and the gradient of first derivatives convergence threshold set to 0.005. The second and third conformational analyses were run for a total of 10000 search steps using Truncated-Newton Conjugate Gradient minimization algorithm (TNCG)¹⁴⁶, with 20000 minimization steps and the gradient of second derivatives convergence threshold set to 0.05. All torsional variables were turned on during the conformational search, with a maximum atom deviation cutoff of 0.8 Å to discriminate between redundant conformers. The energy window for saving structures was set to 20.0 kcal/mol.

Through visual inspection of all the conformers produced by the three conformational runs, we selected 11 structures whose metal binding mode lies in one of the four metal anchoring areas predicted by NMR and CSP measurements (Fig. 1). Three binding modes have been identified: T β 4^{N-N}, in which the metal is bound to the N-terminal of the protein (ASP², ASP⁵, GLU⁸ and GLU¹⁰ residues); T β 4^{N-mid} in which the metal is bound to the N-terminal and the middle of the protein (ASP², ASP⁵, GLU¹⁰ and GLU²⁴ residues); T β 4^{N-C} in which the metal is bound to the N-terminal and the C-terminal regions of the protein (ASP⁵, GLU⁸, GLU²¹ and GLU³⁵ residues).

Five conformers for the T β 4^{N-C} and T β 4^{N-mid} binding modes were chosen, and one for the T β 4^{N-N} binding mode, for a total of eleven initial structures.

Molecular Dynamics simulations

The eleven Fe³⁺-T β 4 structures selected from the previous conformational analyses were immersed in a dodecahedron box with the solute kept to a distance of 20 Å from the box and solvated with \approx 8000 TIP4P-ew¹⁴⁷ water molecules along with a salt concentration of 150 mM NaCl. The protein was modeled with the AMBER99SB*ILDN-Q force field^{148,149} suitable for intrinsically disordered proteins. Although conformational analyses have been performed with Fe³⁺ ion, MD simulations were performed using the Al³⁺ metal ion. This choice is due to the fact iron is a paramagnetic element, therefore NMR and CSP data for Al(III)

(Table 1) are more reliable. Parameters for the Al^{3+} ion were taken from Pengfei Li et al. ¹⁵⁰ as they have been developed for the AMBER family of force fields and the TIP4P-ew water model.

Long range electrostatic interactions were evaluated using particle-mesh Ewald (PME) approach ¹⁵¹ and Lennard-Jones interactions were truncated at 12 Å with an atom based force switching function which is effective at 10 Å. After 5000 steps of steepest descent minimization, the system was equilibrated in a multistep manner with decreasing force constants according to the scheme illustrated in Table S3. Production run was conducted in the NPT ensemble for 1 μs for each run. All atoms were constrained with the LINCS algorithm ¹⁵²; hydrogen atoms were treated as virtual interaction sites so that to allow a time step of 4.0 fs while maintaining energy conservation ¹⁵³. Simulations were performed at the temperature of 310 K and 1.0 atm pressure. The V-rescale thermostat (JCP 126, 014101) with a time constant of 0.1 ps was used to control the temperature. The isotropic Berendsen barostat was used for the equilibration stage, whereas the Parrinello-Rahman one ¹⁵⁴ was used for production runs; the reference pressure was set to 1.0 atm, the time constant to 2.0 ps and the isothermal compressibility to 4.5×10^{-5} in order to maintain the pressure of the system. Dispersion correction was used to correct long range dispersion of energy and pressure.

Cell cultures

Commercial cell line J774 (ICLC ATL98011) was obtained from the Istituto Nazionale per la Ricerca sul Cancro c/o CBA (ICLC, Genova). The culture medium used for this purpose was a mixture of MEM (EBSS), 10% fetal bovine serum (FBS), 100 units/ml penicillin, 100 mg/ml streptomycin, 2 mM L-Glutamine, 1% non-essential amino acids. To perform different experimental conditions, confluent cells were isolated using trypsin/EDTA and, for the experimental procedure, samples of $2-3 \times 10^4$ cells/cm² J774 cells were plated on different glass coverslips at 37°C, 5% CO₂.

TEM Microscopy

Samples of J774 cells used in this study were fixed for 2 hours in a solution of 1% (para)formaldehyde and 1.25% glutaraldehyde in 0.1 M sodium cacodylate buffer, pH 7.4. They were post-fixed in 1% osmium tetroxide for 1 hr and stained in aqueous uranyl acetate 0.25% overnight at 4°C. Cell cultures underwent a dehydration process in an ascending graded series of ethanol and xylene, followed by infiltration and embedding in Embed 812 resin. The specimens were transferred to flat embedding molds and polymerized in the oven at 60°C for 24 hours. 60–90 nm thin sections were cut with an LKB ultratome 8800 ultramicrotome, post-stained with uranyl acetate and bismuth subnitrate, observed and photographed using a transmission electron microscope (JEOL 1400 plus model, Tokyo, Japan) operating at 80 kV.

Gene expression

The expression of the following genes at the mRNA level was evaluated by real time PCR: BAX; HSP70; HO-1 and TXNRD-1. The cells were immediately frozen after treatment and stored at -80°C until RNA extraction. The RNA was extracted with NorDiag ARROW RNA kit using the automated tool of the same company. Actin was used as a reference gene ¹⁵⁵. The Real-time reverse-transcriptase PCR was performed using the Roche Light Cycler system and SYBR Green I kit amplification kit (Roche Diagnostics). The following primers (b-actin ^{1/4} 50 -GCATGGGT CAGAAGG-30, b-actin ^{1/4} 50 -AGGCGTA- CAGGGATAG-30) were designed using the sequences of the human beta-actin mRNA (Gen- Bank accession no. NM_001101).

Real time was performed in 20 μl of final volume contained: 3 mM MgCl₂, 0.25 mM of each primer, and 2 μl of RNA extract. Cycling was performed using the following amplification conditions: an initial reverse transcription at 55°C for 10 min, denaturation at 95°C for 30 s followed by 35 cycles at 95°C for 10s, 53°C for 10 s and 72°C for 8 s with subsequent melting analysis: heating to 95°C for 20 s, cooling to 5°C for 10 s and re-heating to 95°C° per second.

Fluorescence was detected at the end of the 81°C segment in PCR step (single mode) and at 45°C segment in the melting step (continuous mode) in the F1 channel. The relative gene expression was analyzed by using the 2-DDCT method ¹⁵⁶. For each of three analysis, three distinct biological replicas were done, and quantitative data were expressed as a mean. Folding change values in genes expression relative to the beta-actin have been represented as mean + standard error. Statistical comparison of the genes expression in different experimental conditions was performed, with 5.0 GraphPad Prism software, by the unpaired t-test with Welch's correction being the samples size equal, small and the variance unequal. The data were analysed also with one-way ANOVA as well as the multicomparison Tukey's test. P values < 0.05 was considered significant.

Declarations

Acknowledgments

Financial support from FIR 2019 and from Regione Autonoma della Sardegna (grant RASSR79857) is gratefully acknowledged. We acknowledge the CeSAR (Centro Servizi d'Ateneo per la Ricerca) of the University of Cagliari, Italy for the Transmission Electron microscopic analysis performed with the JEOL 1400 plus TEM.

References

1. Low, T. & Goldstein, A. L. Chemical characterization of thymosin beta 4. *Journal of Biological Chemistry*, **257**, 1000–1006 (1982).
2. Dixon, S. J. Ferroptosis: bug or feature? *Immunological reviews*, **277**, 150–157 (2017).
3. Galluzzi, L. *et al.* Molecular mechanisms of cell death: recommendations of the Nomenclature Committee on Cell Death 2018. *Cell Death & Differentiation*, **25**, 486–541 (2018).
4. Dixon, S. J. *et al.* Ferroptosis: an iron-dependent form of nonapoptotic cell death., **149**, 1060–1072 (2012).

5. Yagoda, N. *et al.* RAS–RAF–MEK-dependent oxidative cell death involving voltage-dependent anion channels. *nature*, **447**, 865–869 (2007).
6. Ndayisaba, A., Kaindlstorfer, C. & Wenning, G. K. Iron in neurodegeneration—cause or consequence? *Frontiers in neuroscience*, **13**, 180 (2019).
7. Carbonell, T. & Rama, R. Iron, oxidative stress and early neurological deterioration in ischemic stroke. *Curr. Med. Chem*, **14**, 857–874 (2007).
8. Wang, H. *et al.* Characterization of ferroptosis in murine models of hemochromatosis., **66**, 449–465 (2017).
9. Bogdan, A. R., Miyazawa, M., Hashimoto, K. & Tsuji, Y. Regulators of iron homeostasis: new players in metabolism, cell death, and disease. *Trends in biochemical sciences*, **41**, 274–286 (2016).
10. Cassimeris, L., Safer, D., Nachmias, V. T. & Zigmond, S. Thymosin beta 4 sequesters the majority of G-actin in resting human polymorphonuclear leukocytes. *The Journal of cell biology*, **119**, 1261–1270 (1992).
11. Philp, D. & Kleinman, H. K. Animal studies with thymosin β 4, a multifunctional tissue repair and regeneration peptide. *Annals of the New York Academy of Sciences*, **1194**, 81–86 (2010).
12. Smart, N., Rossdeutsch, A. & Riley, P. R. Thymosin β 4 and angiogenesis: modes of action and therapeutic potential., **10**, 229–241 (2007).
13. Faa, G. *et al.* Thymosin beta-4 prenatal administration improves fetal development and halts side effects due to preterm delivery. *European Review for Medical and Pharmacological Sciences*, **25**, 431–437 (2021).
14. Goldstein, A. L. (Oxford University Press, 2003).
15. Pardon, M. C. Anti-inflammatory potential of thymosin β 4 in the central nervous system: implications for progressive neurodegenerative diseases. *Expert opinion on biological therapy*, **18**, 165–169 (2018).
16. Erickson-Viitanen, S., Ruggieri, S., Natalini, P. & Horecker, B. Distribution of thymosin β 4 in vertebrate classes. *Archives of biochemistry and biophysics*, **221**, 570–576 (1983).
17. Huff, T. *et al.* Nuclear localisation of the G-actin sequestering peptide thymosin β 4. *Journal of cell science*, **117**, 5333–5341 (2004).
18. Piludu, M. *et al.* Thymosin beta 4 may translocate from the cytoplasm in to the nucleus in HepG2 cells following serum starvation. An ultrastructural study. *PloS one*, **10**, e0119642 (2015).
19. Zhang, Y. *et al.* Thymosin Beta 4 is overexpressed in human pancreatic cancer cells and stimulates proinflammatory cytokine secretion and JNK activation. *Cancer biology & therapy*, **7**, 419–423 (2008).
20. Lee, S. Y. *et al.* Increased expression of thymosin β 4 is independently correlated with hypoxia inducible factor-1 α (HIF-1 α) and worse clinical outcome in human colorectal cancer. *Journal of pathology and translational medicine*, **51**, 9 (2017).
21. Wirsching, H. G. *et al.* Thymosin beta 4 gene silencing decreases stemness and invasiveness in glioblastoma., **137**, 433–448 (2014).
22. Huang, D., Wang, S., Wang, A., Chen, X. & Zhang, H. Thymosin beta 4 silencing suppresses proliferation and invasion of non-small cell lung cancer cells by repressing Notch1 activation. *Acta Biochimica et Biophysica Sinica*, **48**, 788–794 (2016).
23. Lachowicz, J. I. *et al.* Metal coordination of thymosin β 4: Chemistry and possible implications. *Coord. Chem. Rev*, **396**, 117–123 (2019).
24. Al-Harathi, S., Lachowicz, J. I., Nowakowski, M. E., Jaremko, M. & Jaremko, Å. Towards the functional high-resolution coordination chemistry of blood plasma human serum albumin. *Journal of inorganic biochemistry*, **198**, 110716 (2019).
25. Zarbock, J. *et al.* Solution conformation of thymosin. beta. 4: a nuclear magnetic resonance and simulated annealing study., **29**, 7814–7821 (1990).
26. Emwas, A. H. *et al.* NMR as a “Gold Standard” Method in Drug Design and Discovery., **25**, 4597 (2020).
27. (https://www.sheffield.ac.uk/polopoly_fs/1.393312!/file/shift_mapping_2013.pdf).
28. Mujika, J. I. *et al.* Aluminum's preferential binding site in proteins: sidechain of amino acids versus backbone interactions. *Journal of inorganic biochemistry*, **181**, 111–116 (2018).
29. Dudev, T. & Lim, C. Metal binding affinity and selectivity in metalloproteins: insights from computational studies. *Annu. Rev. Biophys*, **37**, 97–116 (2008).
30. Torti, S. V. & Torti, F. M. Iron and cancer: more ore to be mined. *Nature Reviews Cancer*, **13**, 342–355 (2013).
31. Cheah, J. H. *et al.* NMDA receptor-nitric oxide transmission mediates neuronal iron homeostasis via the GTPase Dexas1., **51**, 431–440 (2006).
32. Choi, D. W. Glutamate neurotoxicity and diseases of the nervous system., **1**, 623–634 (1988).
33. Murphy, T. H., Miyamoto, M., Sastre, A., Schnaar, R. L. & Coyle, J. T. Glutamate toxicity in a neuronal cell line involves inhibition of cystine transport leading to oxidative stress., **2**, 1547–1558 (1989).
34. Ganz, T. Systemic iron homeostasis. *Physiological reviews*, **93**, 1721–1741 (2013).
35. Cazzola, M., Della Porta, M. G. & Malcovati, L. Clinical relevance of anemia and transfusion iron overload in myelodysplastic syndromes. *ASH Education Program Book*, **2008**, 166–175 (2008).
36. Shenoy, N., Vallumsetla, N., Rachmilewitz, E., Verma, A. & Ginzburg, Y. Impact of iron overload and potential benefit from iron chelation in low-risk myelodysplastic syndrome. *Blood, The Journal of the American Society of Hematology*, **124**, 873–881 (2014).
37. Youssef, L. A. *et al.* Increased erythrophagocytosis induces ferroptosis in red pulp macrophages in a mouse model of transfusion. *Blood, The Journal of the American Society of Hematology*, **131**, 2581–2593 (2018).
38. Imoto, S. *et al.* Haemin-induced cell death in human monocytic cells is consistent with ferroptosis. *Transfusion and Apheresis Science*, **57**, 524–531 (2018).
39. Soares, M. P. & Hamza, I. Macrophages and iron metabolism., **44**, 492–504 (2016).
40. Tan, S., Schubert, D. & Maher, P. Oxytosis: a novel form of programmed cell death. *Current topics in medicinal chemistry*, **1**, 497–506 (2001).

41. Kang, Y., Tiziani, S., Park, G., Kaul, M. & Paternostro, G. Cellular protection using Flt3 and PI3Ka inhibitors demonstrates multiple mechanisms of oxidative glutamate toxicity. *Nature communications*, **5**, 1–12 (2014).
42. Morrison, I. I. B. et al. L-Arginyl-3, 4-Spermidine is neuroprotective in several in vitro models of neurodegeneration and in vivo ischaemia without suppressing synaptic transmission. *British journal of pharmacology*, **137**, 1255–1268 (2002).
43. Sundstrom, L., Pringle, A., Morrison, B. & Bradley, M. Organotypic cultures as tools for functional screening in the CNS. *Drug discovery today*, **10**, 993–1000 (2005).
44. Gomes, A., Fernandes, E. & Lima, J. L. Fluorescence probes used for detection of reactive oxygen species. *Journal of biochemical and biophysical methods*, **65**, 45–80 (2005).
45. Martinez, A. M., Kim, A. & Yang, W. S. in *Immune Mediators in Cancer* 125–130(Springer, 2020).
46. Angeli, J. P. F. et al. Inactivation of the ferroptosis regulator Gpx4 triggers acute renal failure in mice. *Nature cell biology*, **16**, 1180–1191 (2014).
47. Grohm, J., Plesnila, N. & Culmsee, C. Bid mediates fission, membrane permeabilization and peri-nuclear accumulation of mitochondria as a prerequisite for oxidative neuronal cell death. *Brain, behavior, and immunity*, **24**, 831–838 (2010).
48. Jelinek, A. et al. Mitochondrial rescue prevents glutathione peroxidase-dependent ferroptosis. *Free Radical Biology and Medicine*, **117**, 45–57 (2018).
49. Neitemeier, S. et al. BID links ferroptosis to mitochondrial cell death pathways. *Redox biology*, **12**, 558–570 (2017).
50. Wang, H., Liu, C., Zhao, Y. & Gao, G. Mitochondria regulation in ferroptosis. *European Journal of Cell Biology*, **99**, 151058 (2020).
51. Gerdes, H. H. & Carvalho, R. N. Intercellular transfer mediated by tunneling nanotubes. *Current opinion in cell biology*, **20**, 470–475 (2008).
52. Davis, D. M. & Sowinski, S. Membrane nanotubes: dynamic long-distance connections between animal cells. *Nature Reviews Molecular Cell Biology*, **9**, 431–436 (2008).
53. Zhu, D. et al. Hydrogen peroxide alters membrane and cytoskeleton properties and increases intercellular connections in astrocytes. *Journal of cell science*, **118**, 3695–3703 (2005).
54. Luchetti, F. et al. Fas signaling promotes intercellular communication in T cells. *PLoS one*, **7**, e35766 (2012).
55. Stockwell, B. R. et al. Ferroptosis: a regulated cell death nexus linking metabolism, redox biology, and disease., **171**, 273–285 (2017).
56. Hou, Q. & Hsu, Y. T. Bax translocates from cytosol to mitochondria in cardiac cells during apoptosis: development of a GFP-Bax-stable H9c2 cell line for apoptosis analysis. *American Journal of Physiology-Heart and Circulatory Physiology*, **289**, H477–H487 (2005).
57. Jungas, T. et al. Glutathione levels and BAX activation during apoptosis due to oxidative stress in cells expressing wild-type and mutant cystic fibrosis transmembrane conductance regulator. *Journal of Biological Chemistry*, **277**, 27912–27918 (2002).
58. Chen, J. et al. Expression of the apoptosis-effector gene, Bax, is up-regulated in vulnerable hippocampal CA1 neurons following global ischemia. *Journal of neurochemistry*, **67**, 64–71 (1996).
59. Krajewski, S. et al. Upregulation of bax protein levels in neurons following cerebral ischemia. *Journal of Neuroscience*, **15**, 6364–6376 (1995).
60. Guo, S., Wharton, W., Moseley, P. & Shi, H. Heat shock protein 70 regulates cellular redox status by modulating glutathione-related enzyme activities. *Cell stress & chaperones*, **12**, 245 (2007).
61. Papadopoulos, M. C., Sun, X. Y., Cao, J., Mivechi, N. F. & Giffard, R. G. Over-expression of HSP-70 protects astrocytes from combined oxygen-glucose deprivation., **7**, 429–432 (1996).
62. Plumier, J. C. et al. Transgenic mice expressing the human inducible Hsp70 have hippocampal neurons resistant to ischemic injury. *Cell stress & chaperones*, **2**, 162 (1997).
63. Aufricht, C. et al. ATP releases HSP-72 from protein aggregates after renal ischemia. *American Journal of Physiology-Renal Physiology*, **274**, F268–F274 (1998).
64. Bidmon, B. et al. Heat shock protein-70 repairs proximal tubule structure after renal ischemia. *Kidney international*, **58**, 2400–2407 (2000).
65. Calabrese, V. et al. Nitric oxide synthase induction in astroglial cell cultures: effect on heat shock protein 70 synthesis and oxidant/antioxidant balance. *Journal of neuroscience research*, **60**, 613–622 (2000).
66. McLaughlin, B. et al. Caspase 3 activation is essential for neuroprotection in preconditioning. *Proceedings of the National Academy of Sciences* **100**, 715–720(2003).
67. Yan, L. J. et al. Mouse heat shock transcription factor 1 deficiency alters cardiac redox homeostasis and increases mitochondrial oxidative damage. *The EMBO journal*, **21**, 5164–5172 (2002).
68. Chiang, S. K., Chen, S. E. & Chang, L. C. A dual role of heme oxygenase-1 in cancer cells. *International Journal of Molecular Sciences*, **20**, 39–57 (2018).
69. Jozkowicz, A., Was, H. & Dulak, J. Heme oxygenase-1 in tumors: is it a false friend? *Antioxidants & redox signaling*, **9**, 2099–2118 (2007).
70. Hsu, Y. Y., Chen, C. S., Wu, S. N., Jong, Y. J. & Lo, Y. C. Berberine activates Nrf2 nuclear translocation and protects against oxidative damage via a phosphatidylinositol 3-kinase/Akt-dependent mechanism in NSC34 motor neuron-like cells. *European Journal of Pharmaceutical Sciences*, **46**, 415–425 (2012).
71. Kwon, M. Y., Park, E., Lee, S. J. & Chung, S. W. Heme oxygenase-1 accelerates erastin-induced ferroptotic cell death. *Oncotarget*, **6**, 24393 (2015).
72. Sun, X. et al. Activation of the p62-Keap1-NRF2 pathway protects against ferroptosis in hepatocellular carcinoma cells., **63**, 173–184 (2016).
73. Gasdaska, P. Y., Gasdaska, J. R., Cochran, S. & Powis, G. Cloning and sequencing of a human thioredoxin reductase. *FEBS Letters*, **373**, 5–9 (1995).
74. Cai, L. L. et al. Modulation of ferroptosis sensitivity by TXNRD1 in pancreatic cancer cells. *bioRxiv*(2020).

75. Yang, L. *et al.* Auranofin mitigates systemic iron overload and induces ferroptosis via distinct mechanisms. *Signal transduction and targeted therapy*, **5**, 1–9 (2020).
76. Low, T. L. & Mercer, R. C. Isolation and structural studies of porcine, ovine and murine thymosin β 4 by high-performance liquid chromatography. *Journal of Chromatography A*, **301**, 221–239 (1984).
77. Snyder, W. *et al.* Report of the task group on reference man. Vol. 23(Pergamon Oxford, 1975).
78. Forciniti, S., Greco, L., Grizzi, F., Malesci, A. & Laghi, L. Iron metabolism in cancer progression. *International Journal of Molecular Sciences*, **21**, 2257 (2020).
79. Rebours, V. *et al.* In situ proteomic analysis by MALDI imaging identifies ubiquitin and thymosin- β 4 as markers of malignant intraductal pancreatic mucinous neoplasms. *Pancreatology* **14**, 117–124(2014).
80. Chen, G., Guo, G., Zhou, X. & Chen, H. Potential mechanism of ferroptosis in pancreatic cancer. *Oncology letters*, **19**, 579–587 (2020).
81. Theunissen, W. *et al.* Thymosin beta 4 and thymosin beta 10 expression in hepatocellular carcinoma. *European journal of histochemistry: EJH*, **58**, 2242 (2014).
82. Nie, J., Lin, B., Zhou, M., Wu, L. & Zheng, T. Role of ferroptosis in hepatocellular carcinoma. *Journal of cancer research and clinical oncology*, **144**, 2329–2337 (2018).
83. Can, B. *et al.* Thymosin β 4 is a novel potential prognostic marker in gastrointestinal stromal tumors. *Apmis*, **120**, 689–698 (2012).
84. Song, Y., Yang, H., Lin, R., Jiang, K. & Wang, B. M. The role of ferroptosis in digestive system cancer. *Oncology letters*, **18**, 2159–2164 (2019).
85. Ji, Y. I. *et al.* Expression patterns of thymosin β 4 and cancer stem cell marker cd133 in ovarian cancers. *Pathology & Oncology Research*, **19**, 237–245 (2013).
86. Sui, X. *et al.* RSL3 drives ferroptosis through GPX4 inactivation and ROS production in colorectal cancer. *Frontiers in pharmacology*, **9**, 1371 (2018).
87. Larsson, L. I. & Holck, S. Occurrence of thymosin β 4 in human breast cancer cells and in other cell types of the tumor microenvironment. *Human pathology*, **38**, 114–119 (2007).
88. Yoon, S. Y. *et al.* Thymosin β 4 expression correlates with lymph node metastasis through hypoxia inducible factor- α induction in breast cancer. *Oncology reports*, **25**, 23–31 (2011).
89. Ma, S., Henson, E., Chen, Y. & Gibson, S. Ferroptosis is induced following siramesine and lapatinib treatment of breast cancer cells. *Cell death & disease*, **7**, e2307–e2307 (2016).
90. Alvarez, S. W. *et al.* NFS1 undergoes positive selection in lung tumours and protects cells from ferroptosis. *nature* **551**, 639–643(2017).
91. Lin, C. C. & Chi, J. T. Ferroptosis of epithelial ovarian cancer: genetic determinants and therapeutic potential. *Oncotarget*, **11**, 3562 (2020).
92. Kim, A. *et al.* Elevation of intracellular cyclic AMP inhibits NF- κ B-mediated thymosin β 4 expression in melanoma cells. *Experimental cell research*, **315**, 3325–3335 (2009).
93. Makowiecka, A. *et al.* Thymosin β 4 regulates focal adhesion formation in human melanoma cells and affects their migration and invasion. *Frontiers in cell and developmental biology*, **7**, 304 (2019).
94. Gagliardi, M. *et al.* Ferroptosis: a new unexpected chance to treat metastatic melanoma?, **19**, 2411–2425 (2020).
95. Chi, L. H. *et al.* Global proteomics-based identification and validation of thymosin Beta-4 X-linked as a prognostic marker for head and neck squamous cell carcinoma. *Scientific reports*, **7**, 1–13 (2017).
96. Roh, J. L., Kim, E. H., Jang, H. J., Park, J. Y. & Shin, D. Induction of ferroptotic cell death for overcoming cisplatin resistance of head and neck cancer. *Cancer letters*, **381**, 96–103 (2016).
97. Sapp, E. *et al.* Early and progressive accumulation of reactive microglia in the Huntington disease brain. *Journal of Neuropathology & Experimental Neurology*, **60**, 161–172 (2001).
98. Gao, M., Monian, P., Quadri, N., Ramasamy, R. & Jiang, X. Glutaminolysis and transferrin regulate ferroptosis. *Molecular cell*, **59**, 298–308 (2015).
99. Linkermann, A. *et al.* Synchronized renal tubular cell death involves ferroptosis. *Proceedings of the National Academy of Sciences* **111**, 16836–16841(2014).
100. Skouta, R. *et al.* Ferrostatins inhibit oxidative lipid damage and cell death in diverse disease models. *Journal of the American Chemical Society*, **136**, 4551–4556 (2014).
101. Tuo, Q. *et al.* Tau-mediated iron export prevents ferroptotic damage after ischemic stroke. *Molecular psychiatry*, **22**, 1520–1530 (2017).
102. Chen, L., Hambricht, W. S., Na, R. & Ran, Q. Ablation of the ferroptosis inhibitor glutathione peroxidase 4 in neurons results in rapid motor neuron degeneration and paralysis. *Journal of Biological Chemistry*, **290**, 28097–28106 (2015).
103. Do Van, B. *et al.* Ferroptosis, a newly characterized form of cell death in Parkinson's disease that is regulated by PKC. *Neurobiology of disease*, **94**, 169–178 (2016).
104. Gascón, S. *et al.* Identification and successful negotiation of a metabolic checkpoint in direct neuronal reprogramming. *Cell stem cell*, **18**, 396–409 (2016).
105. Guiney, S. J., Adlard, P. A., Bush, A. I., Finkelstein, D. I. & Ayton, S. Ferroptosis and cell death mechanisms in Parkinson's disease. *Neurochemistry international*, **104**, 34–48 (2017).
106. Hambricht, W. S., Fonseca, R. S., Chen, L., Na, R. & Ran, Q. Ablation of ferroptosis regulator glutathione peroxidase 4 in forebrain neurons promotes cognitive impairment and neurodegeneration. *Redox biology*, **12**, 8–17 (2017).
107. Li, Q. *et al.* Inhibition of neuronal ferroptosis protects hemorrhagic brain. *JCI insight* **2** (2017).

108. Zille, M. *et al.* Neuronal death after hemorrhagic stroke in vitro and in vivo shares features of ferroptosis and necroptosis., **48**, 1033–1043 (2017).
109. Goldstein, A. L., Hannappel, E., Sosne, G. & Kleinman, H. K. Thymosin β 4: a multi-functional regenerative peptide. Basic properties and clinical applications. *Expert opinion on biological therapy*, **12**, 37–51 (2012).
110. Morris, D. C., Chopp, M., Zhang, L., Lu, M. & Zhang, Z. G. Thymosin β 4 improves functional neurological outcome in a rat model of embolic stroke., **169**, 674–682 (2010).
111. Xiong, Y. *et al.* Treatment of traumatic brain injury with thymosin β 4 in rats. *Journal of neurosurgery*, **114**, 102–115 (2011).
112. Zhang, J. *et al.* Neurological functional recovery after thymosin β 4 treatment in mice with experimental auto encephalomyelitis., **164**, 1887–1893 (2009).
113. Wang, L. *et al.* Thymosin β 4 promotes the recovery of peripheral neuropathy in type II diabetic mice. *Neurobiology of disease*, **48**, 546–555 (2012).
114. DeGregorio-Rocasolano, N., Martí-Sistac, O. & Gasull, T. Deciphering the iron side of stroke: neurodegeneration at the crossroads between iron dyshomeostasis, excitotoxicity, and ferroptosis. *Frontiers in neuroscience*, **13**, 85 (2019).
115. Ren, J. X., Sun, X., Yan, X. L., Guo, Z. N. & Yang, Y. Ferroptosis in neurological diseases. *Frontiers in Cellular Neuroscience* **14** (2020).
116. Weiland, A. *et al.* Ferroptosis and its role in diverse brain diseases. *Mol. Neurobiol*, **56**, 4880–4893 (2019).
117. Vartiainen, N., Pyykönen, I., Hökfelt, T. & Koistinaho, J. Induction of thymosin β 4 mRNA following focal brain ischemia., **7**, 1613–1616 (1996).
118. Wang, J. H. *et al.* Identification of differentially expressed genes of acute hypoxia-treated HepG2 cells and hypoxia-acclimatized HepG2 cells. *Sheng li xue bao: [Acta physiologica Sinica]*, **55**, 324–330 (2003).
119. Kenny, E. M. *et al.* Ferroptosis contributes to neuronal death and functional outcome after traumatic brain injury. *Critical care medicine*, **47**, 410 (2019).
120. Magtanong, L. & Dixon, S. J. Ferroptosis and brain injury. *Developmental neuroscience*, **40**, 382–395 (2018).
121. Tang, S. *et al.* The Role of Iron, Its Metabolism and Ferroptosis in Traumatic Brain Injury. *Frontiers in Cellular Neuroscience*, **14**, 317 (2020).
122. Bock-Marquette, I., Saxena, A., White, M. D., DiMaio, J. M. & Srivastava, D. Thymosin β 4 activates integrin-linked kinase and promotes cardiac cell migration, survival and cardiac repair. *nature* **432**, 466–472(2004).
123. Park, T. J. *et al.* Quantitative proteomic analyses reveal that GPX4 downregulation during myocardial infarction contributes to ferroptosis in cardiomyocytes. *Cell death & disease*, **10**, 1–15 (2019).
124. Li, W., Li, W., Leng, Y., Xiong, Y. & Xia, Z. Ferroptosis is involved in diabetes myocardial ischemia/reperfusion injury through endoplasmic reticulum stress. *DNA and Cell Biology*, **39**, 210–225 (2020).
125. Zhang, Z., Liu, S. & Huang, S. Effects of thymosin β 4 on neuronal apoptosis in a rat model of cerebral ischemia–reperfusion injury. *Molecular medicine reports*, **20**, 4186–4192 (2019).
126. Crockford, D. Development of thymosin β 4 for treatment of patients with ischemic heart disease. *Annals of the New York Academy of Sciences*, **1112**, 385–395 (2007).
127. El-Aouni, C. *et al.* Thymosin β 4 is an essential paracrine factor of embryonic endothelial progenitor cell-mediated cardioprotection., **117**, 2232–2240 (2008).
128. Guan, X. *et al.* Galangin attenuated cerebral ischemia reperfusion injury by inhibition of ferroptosis through activating the SLC7A11/GPX4 axis in gerbils. *Life sciences*, **264**, 118660 (2021).
129. Guan, X. *et al.* The neuroprotective effects of carvedilol on ischemia/reperfusion-induced hippocampal neuronal impairment by ferroptosis mitigation. *Life sciences*, **235**, 116795 (2019).
130. Xing, J., HAN, T. & ZHU Z.-y. Serum thymosin β 4 level in patients with hepatocellular carcinoma. *Journal of clinical hepatology*, **27**, 387–390 (2011).
131. Li, X. *et al.* Thymosin β 4 Alleviates Mouse Liver Ischemia-Reperfusion Injury by Activating AKT-Bad Pathway.: Abstract# P-23. *Liver Transplantation* **18** (2012).
132. Li, X., Wang, L. & Chen, C. Effects of exogenous thymosin β 4 on carbon tetrachloride-induced liver injury and fibrosis. *Scientific reports*, **7**, 1–13 (2017).
133. Chen, L. D. *et al.* The role of ferroptosis in chronic intermittent hypoxia-induced liver injury in rats. *Sleep and Breathing*, **1–7**(2020).
134. Mao, L. *et al.* The emerging role of ferroptosis in non-cancer liver diseases: hype or increasing hope? *Cell death & disease*, **11**, 1–12 (2020).
135. Hametner, S. *et al.* Iron and neurodegeneration in the multiple sclerosis brain. *Annals of neurology*, **74**, 848–861 (2013).
136. Muhoberac, B. B. & Vidal, R. Abnormal iron homeostasis and neurodegeneration. *Frontiers in aging neuroscience*, **5**, 32 (2013).
137. Yang, W. S. & Stockwell, B. R. Ferroptosis: death by lipid peroxidation. *Trends in cell biology*, **26**, 165–176 (2016).
138. Alghrably, M. *et al.* Copper(II) and Amylin Analogues: A Complicated Relationship. *Inorg. Chem*, **59**, 2527–2535 <https://doi.org/10.1021/acs.inorgchem.9b03498> (2020).
139. Sharfalddin, A. A., Emwas, A. H., Jaremko, M. & Hussien, M. A. Transition metal complexes of 6-mercaptopurine: Characterization, Theoretical calculation, DNA-Binding, molecular docking, and anticancer activity. *Applied Organometallic Chemistry*, doi:10.1002/aoc.6041.
140. Glasoe, P. K. & Long, F. Use of glass electrodes to measure acidities in deuterium oxide¹, 2. *The Journal of physical chemistry*, **64**, 188–190 (1960).
141. Willker, W., Wollborn, U. & Leibfritz, D. Exact measurement of ³JCH coupling constants using proton-detected editing and selection sequences. *Journal of Magnetic Resonance, Series B*, **101**, 83–86 (1993).
142. Jorgensen, W. L., Maxwell, D. S. & Tirado-Rives, J. Development and testing of the OPLS all-atom force field on conformational energetics and properties of organic liquids. *Journal of the American Chemical Society*, **118**, 11225–11236 (1996).
143. MacroModel, Schrödinger, L. L. C. (New York, NY, 2020).

144. Chang, G., Guida, W. C. & Still, W. C. An internal-coordinate Monte Carlo method for searching conformational space. *Journal of the American Chemical Society*, **111**, 4379–4386 (1989).
145. Polak, E. & Ribiere, G. Note sur la convergence de méthodes de directions conjuguées. *ESAIM: Mathematical Modelling and Numerical Analysis-Modélisation Mathématique et Analyse Numérique*, **3**, 35–43 (1969).
146. Ponder, J. W. & Richards, F. M. An efficient newton-like method for molecular mechanics energy minimization of large molecules. *Journal of Computational Chemistry*, **8**, 1016–1024 (1987).
147. Horn, H. W. *et al.* Development of an improved four-site water model for biomolecular simulations: TIP4P-Ew. *The Journal of chemical physics*, **120**, 9665–9678 (2004).
148. Best, R. B. & Hummer, G. Optimized molecular dynamics force fields applied to the helix – coil transition of polypeptides. *The Journal of Physical Chemistry B*, **113**, 9004–9015 (2009).
149. Lindorff-Larsen, K. *et al.* Improved side-chain torsion potentials for the Amber ff99SB protein force field. *Proteins: Structure, Function, and Bioinformatics*, **78**, 1950–1958 (2010).
150. Li, P., Song, L. F. & Merz, K. M. Jr Parameterization of highly charged metal ions using the 12-6-4 LJ-type nonbonded model in explicit water. *The Journal of Physical Chemistry B*, **119**, 883–895 (2015).
151. Darden, T., York, D. & Pedersen, L. Particle mesh Ewald: An $N \cdot \log(N)$ method for Ewald sums in large systems. *The Journal of chemical physics*, **98**, 10089–10092 (1993).
152. Hess, B., Bekker, H., Berendsen, H. J. & Fraaije, J. G. LINCS: a linear constraint solver for molecular simulations. *Journal of Computational Chemistry*, **18**, 1463–1472 (1997).
153. Feenstra, K. A., Hess, B. & Berendsen, H. J. Improving efficiency of large time-scale molecular dynamics simulations of hydrogen-rich systems. *Journal of Computational Chemistry*, **20**, 786–798 (1999).
154. Parrinello, M. & Rahman, A. Polymorphic transitions in single crystals: A new molecular dynamics method. *Journal of Applied physics*, **52**, 7182–7190 (1981).
155. Durzyńska, J. & Barton, E. IGF expression in HPV-related and HPV-unrelated human cancer cells. *Oncology reports*, **32**, 893–900 (2014).
156. Livak, K. J. & Schmittgen, T. D. Analysis of relative gene expression data using real-time quantitative PCR and the $2^{-\Delta\Delta CT}$ method., **25**, 402–408 (2001).

Figures

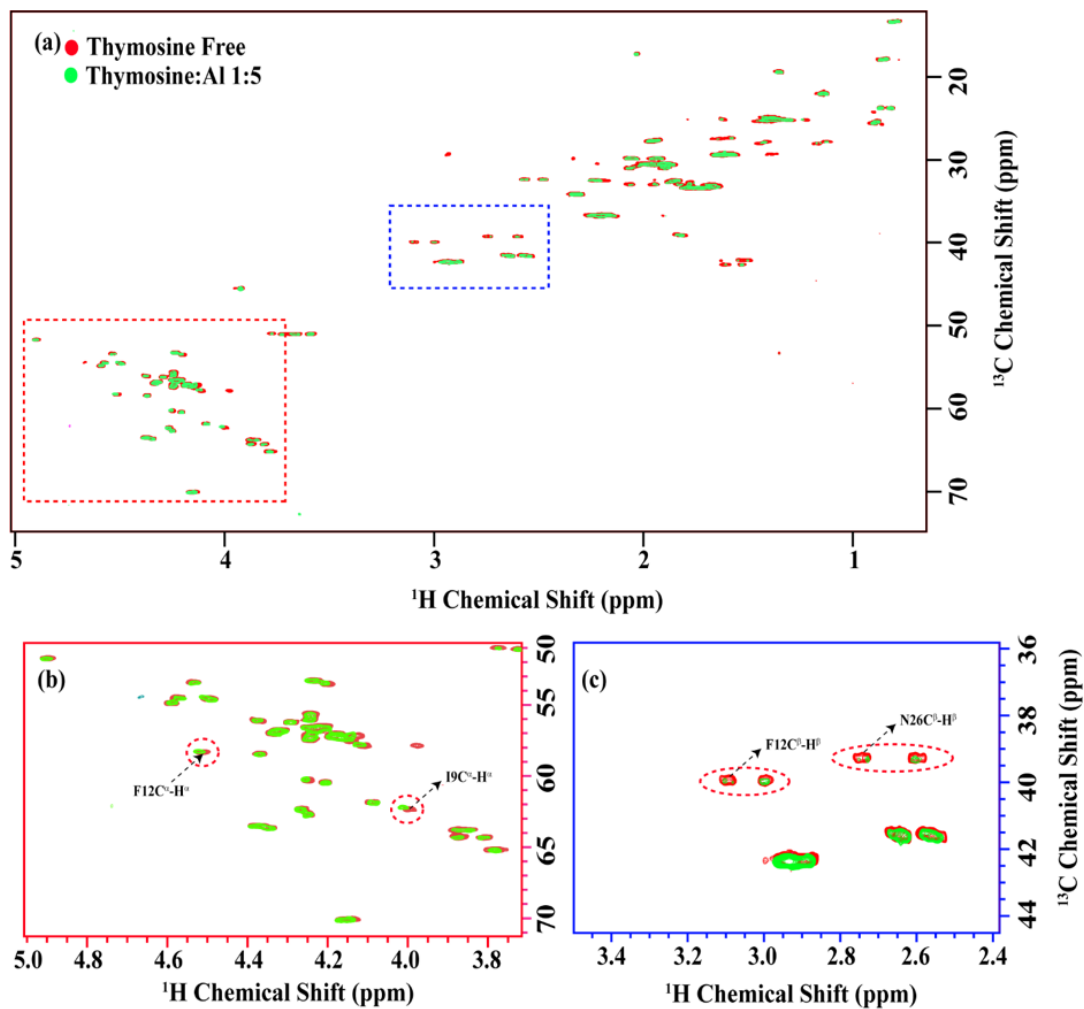


Figure 1

(a) The overlay of the two-dimensional ^{13}C - ^1H HSQC spectra in free form (red) and with Thymosin: Al³⁺ ratio 1:5 (green). The alpha and beta proton regions are highlighted in the red and blue dotted rectangles in (a) and are presented in (b) and (c) respectively. Noticeable chemical shift changes were observed for F12, I9 as indicated by red circles in (b). Otherwise, the chemical shifts remain the same, with only some decrease in the intensities, as highlighted by the red circles in (c).

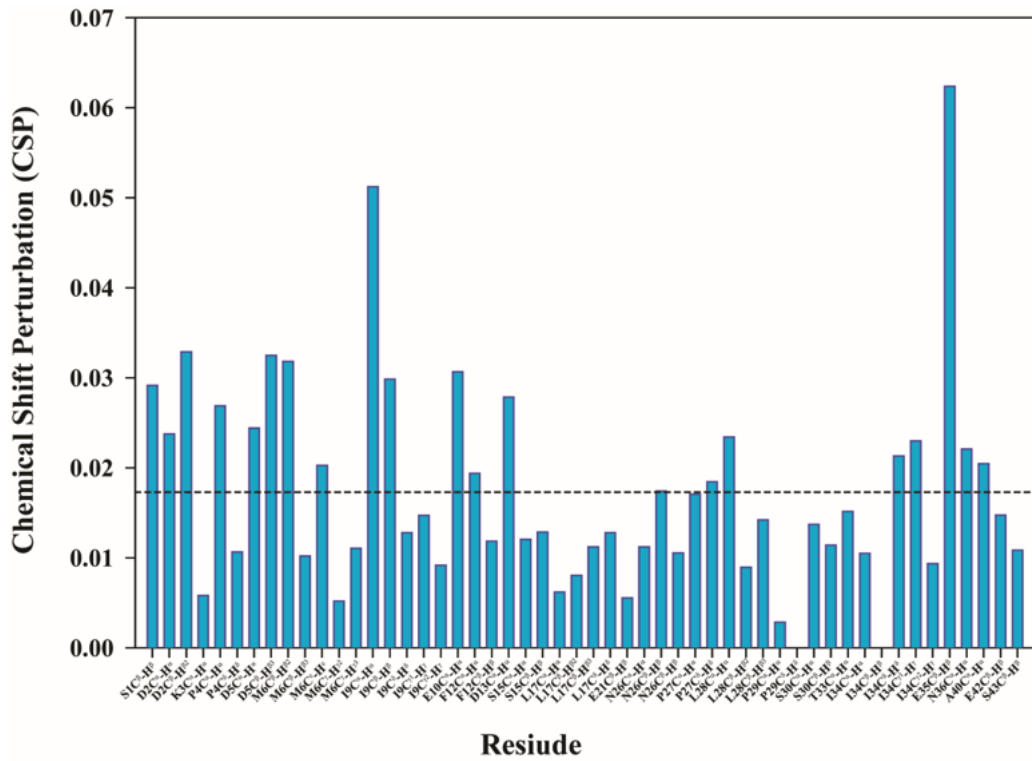


Figure 2

The chemical shift perturbation (CSP) plot for the 48 distinct residues from the overlay of the two-dimensional ^{13}C - ^1H HSQC spectra in free form and with Thymosin: $\text{A}\beta$ ratio 1:5 as indicated in Figure 4. The formula used for CSP is $\text{Sqrt}[1/2(\delta\text{H}2 + \alpha*\delta^{13}\text{C}2)]$ as suggested by Williamson 27. The α was kept 0.3.

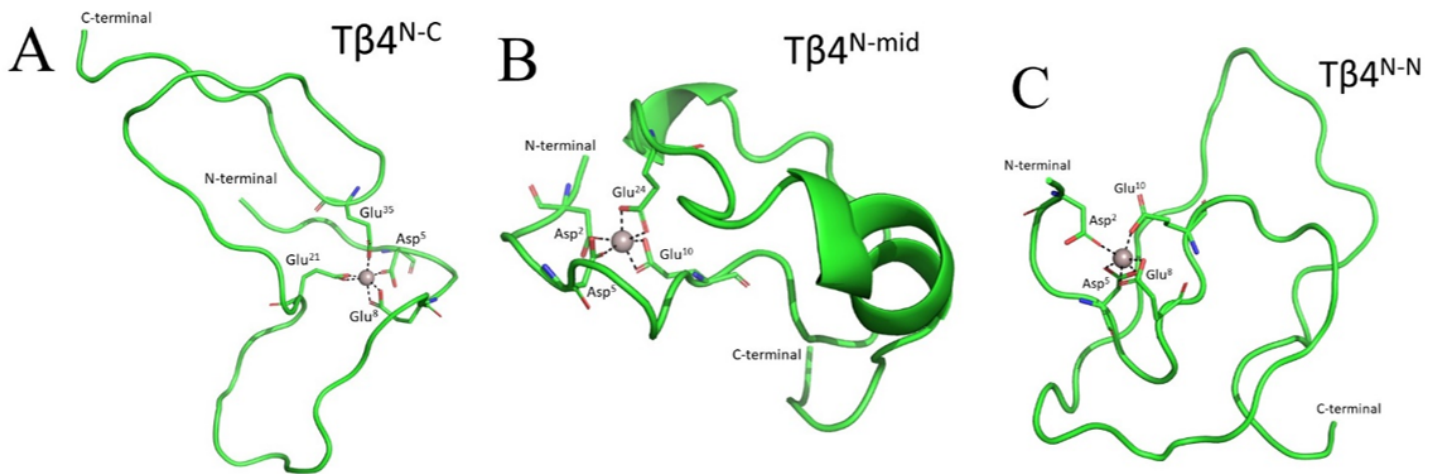


Figure 3

Representative structures of A) Tβ4N-C; B) Tβ4N-mid and C) Tβ4N-N.

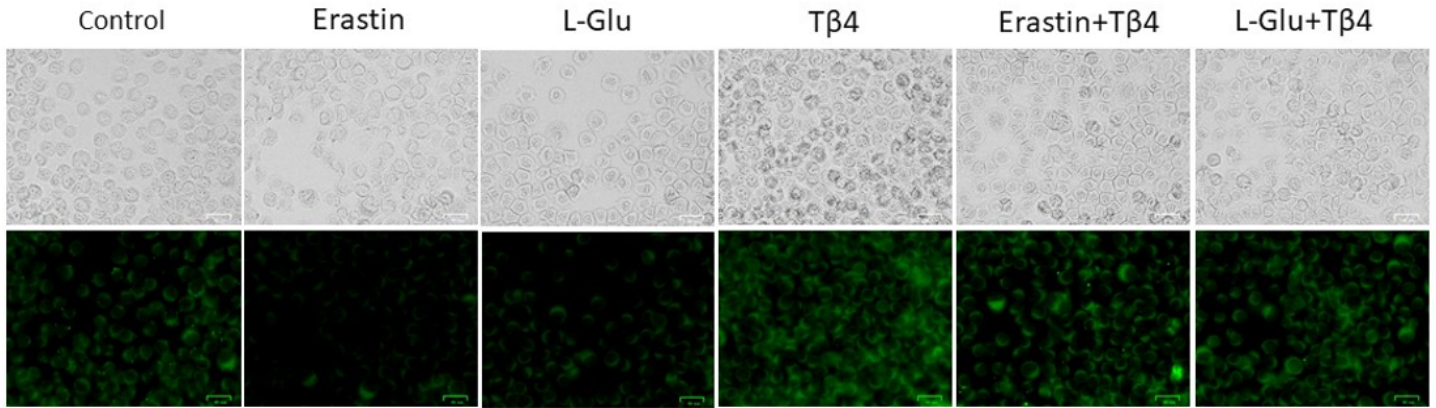


Figure 4
 Bright field (upper) and green field (lower) images of the J774 culture cells placed under different experimental conditions for 24h: Erastin 0.5 [μ M], glutamate (L-Glu) 5.5 [mM], and Thymosin ($T\beta$ 4) 10 [μ M]. C11-BODIPY581/591 was used as a fluorescent probe (λ_{ex} =510 nm; λ_{em} =595 nm) according to published procedure 45.

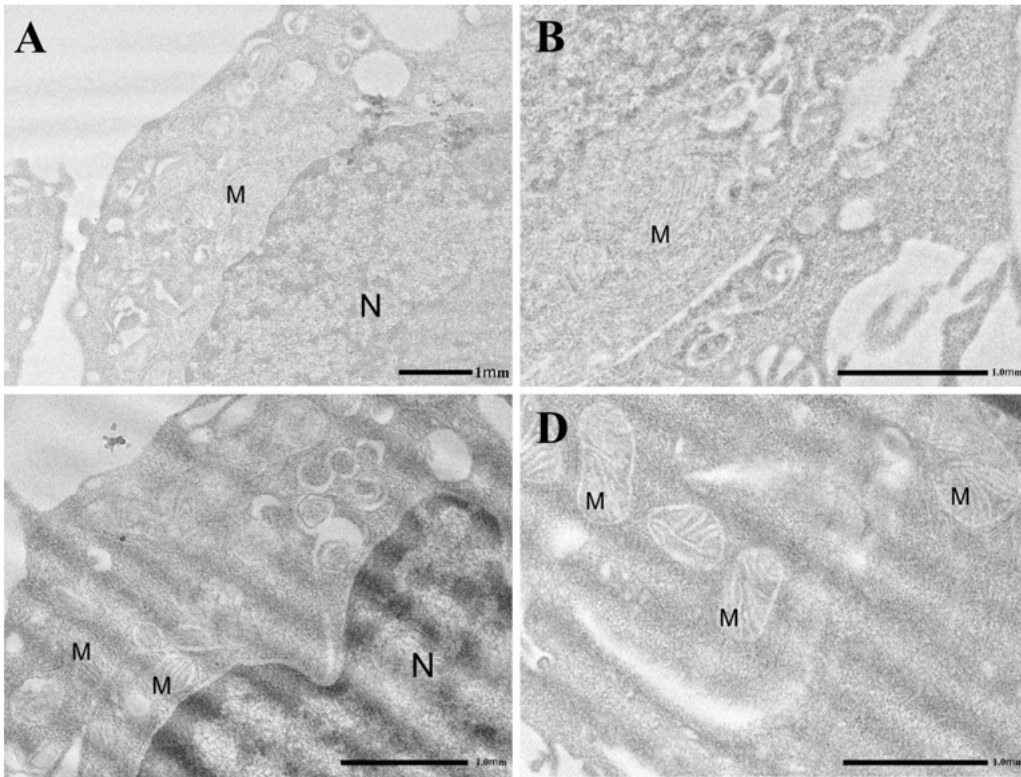


Figure 5
 Electron micrographs of J774cells. (A, B) Control group displays a well-preserved ultrastructure. (C, D) Administration of $T\beta$ 4 (10 μ M, 24 h) does not appear to alter cell morphology. Note in both control and $T\beta$ 4 treated samples the presence of several mitochondria showing a continuous mitochondria membrane and well-organized cristae. M= mitochondria, N= nucleus.

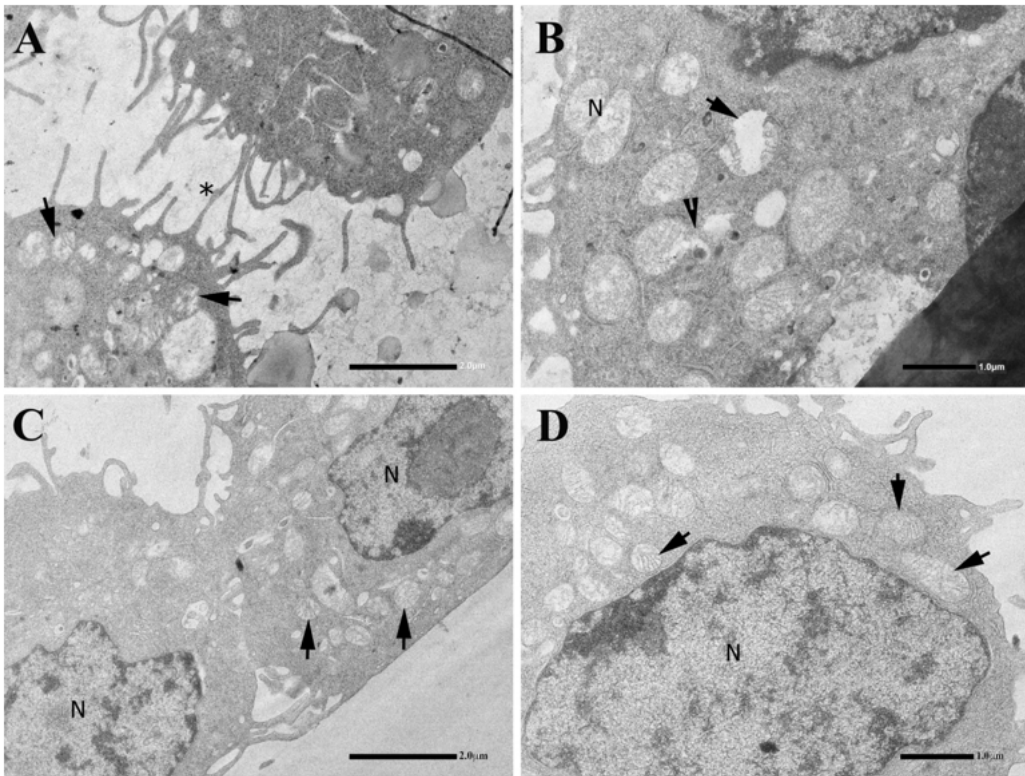


Figure 6
 (A, B) Glutamate treatment (5.5 mM, 24 h) induces numerous cellular alterations that affect especially the mitochondria (arrows). Initially it appears that the membranes of the mitochondria open up, letting the contents pour out (arrowhead). Note the presence of tunnelling nanotubes connecting adjacent cells (asterisk). (C, D) After Tβ4 administration (10 μM, 20 h), the cytoplasmic compartment displays more preserved cell structures. Mitochondria show a continuous mitochondrial membrane and partially reorganized cristae. N= nucleus

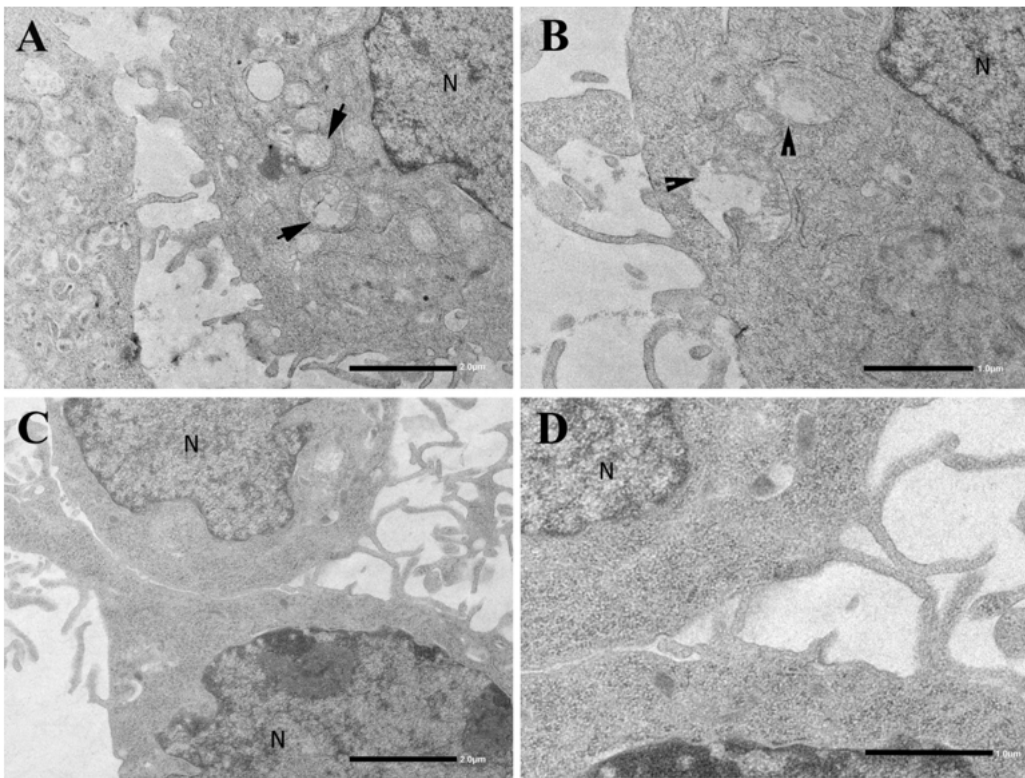


Figure 7

Page 20/21

(A, B) Erastin treatment (0.5 μ M; 24 h) induces numerous cellular alterations that affect especially the mitochondria (arrows). Mitochondria are frequently observed with ruptured mitochondrial membrane and altered cristae (arrowheads). (C, D) After T β 4 administration (10 μ M, 20 h), the cytoplasmic compartment displays more preserved cell structures associated with an evident decrease in lysosomal activity. N= nucleus.

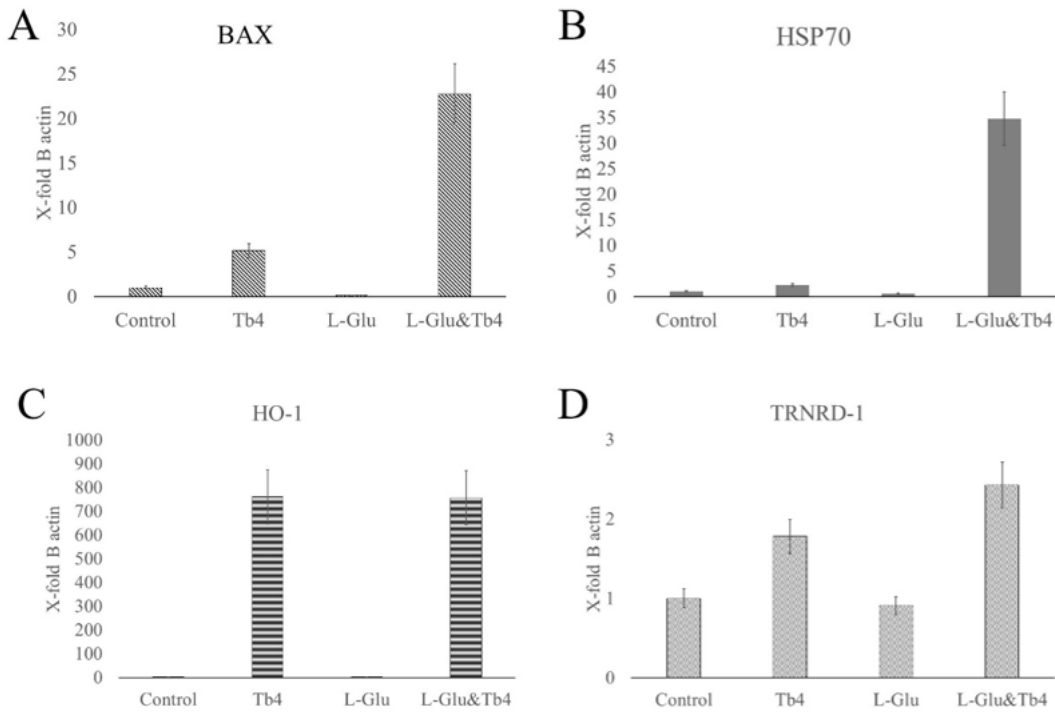


Figure 8
mRNA expression levels (mean and standard error) of A) BAX and HSP70 B) HO-1 and C) TRNRD-1, which are related to stress conditions, in J774 cells. The amount of mRNA of each gene for each experiment was normalized with the respective value of the beta actin housekeeping gene mRNA (X-fold of beta actin expression).

Supplementary Files

This is a list of supplementary files associated with this preprint. Click to download.

- [ThymosinpaperSupplementaryMaterialLachowicz.docx](#)
- [schema1.png](#)
- [schema2.png](#)
- [schema3.png](#)